FILTER AND GRID RESOLUTION REQUIREMENTS IN LES VIA A DISCONTINUOUS GALERKIN SOLVER

by

Ling Miao

B.S. in Aeronautic Science and Engineering, Beihang University (BUAA), Beijing, 2011

M.S. in Mechanical Engineering, Carnegie Mellon University, 2013

Submitted to the Graduate Faculty of

the Swanson School of Engineering in partial fulfillment

of the requirements for the degree of

Doctor of Philosophy

University of Pittsburgh

2018

UNIVERSITY OF PITTSBURGH

SWANSON SCHOOL OF ENGINEERING

This dissertation was presented

by

Ling Miao

It was defended on

July 2, 2018

and approved by

Peyman Givi, Ph.D., Distinguished Professor and James T. MacLeod Professor

Hessameddin Babaee, Ph.D., Assistant Professor

Anne Robertson, Ph.D., William Kepler Whiteford Professor

Mehrdad Massoudi, Ph.D., Adjunct Professor, Department of Mechanical Engineering,

Carnegie Mellon University

Shervin Sammak, Ph.D., Research Assistant Professor, Center for Research Computing

Dissertation Advisors: Peyman Givi, Ph.D., Distinguished Professor and James T.

MacLeod Professor,

Shervin Sammak, Ph.D., Research Assistant Professor, Center for Research Computing

FILTER AND GRID RESOLUTION REQUIREMENTS IN LES VIA A DISCONTINUOUS GALERKIN SOLVER

Ling Miao, PhD

University of Pittsburgh, 2018

The discontinuous Galerkin (DG) methodology has proven very effective for large eddy simulation (LES) of various turbulent flows. In LES with a given discretization accuracy, two important parameters are the grid resolution h and the filter size Δ. In most of the previous works, the grid spacing is usually set to be proportional to the specified filter size. In this work, the DG method is combined with a subgrid scale (SGS) closure which is equivalent to that of the filtered density function (FDF). Various Δ/h ratios for LES of a two-dimensional and three-dimensional temporally developing mixing layer are considered, and a systematic parametric study is conducted to investigate the effects of grid resolution, the filter width size, and the order of the spectral discretization. Comparative assessments are made via the use of high resolution direct numerical simulation (DNS) data.

Keywords: Discontinuous Galerkin; Large eddy simulation; LES filter size; Subgrid scale model; Turbulent flows; Turbulence resolution length scale.

TABLE OF CONTENTS

LIST OF FIGURES

NOMENCLATURE

Roman

C	ratio of filter size to grid resolution
C_ϕ	constant in the FDF model
C_{ν_1}, C_{ν_2}	Smagorinsky constants
F_L	FDF
G	filter function
h	grid resolution
J_j	scalar flux
$\mathcal{L}$	Legendre polynomial
L	simulation domain length
L_r	reference length
M_{ij}	subgrid mass fluxes
N	number of points in y-direction
n_p	number of vortex pairings
P	pressure
p	polynomial degree
R	resolved stresses
r	total stresses
Re	Reynolds number
S_{ij}	strain rate tensor
Sc	Schmidt number
Sc_t	turbulent Schmidt number

t	time
T_{ij}	viscous stress tensor
u_i	velocity vector
U_r	refenrece velocity
W_i	Wierner-Levy process
x, y, z	stream-wise, cross-stream, span-wise flow directions
x_i or $\mathbf{x}$	position vector

Greek

$\boldsymbol{\psi}$, ψ	composition domain of the scalar array
ΔU	velocity difference across the layer
Δ	LES filter size
δ	Dirac delta function
δ_v	initial vorticity thickness
η	computational space coordinate
γ	molecular diffusivity coefficient
γ_t	SGS diffusivity coefficient
λ_u	initial wavelength of the most unstable mode
μ	dynamic viscosity of fluid
μ_t	SGS viscosity
Ω_m	SGS mixing frequency
ϕ	scalar mass fraction
ρ	density
Σ_{ij}	SGS stresses
τ	SGS variance
ζ	fine-grained density

Superscripts

A^+	probabilistic representations

Subscripts

A_{DNS}	quantity A in DNS
A_{LES}	quantity A in LES

Symbols

$\langle \vert \rangle_\ell$	conditional filtered value
$\langle \rangle_\ell$, $\langle \rangle$	filtered value
$\langle \rangle_L$	Favré-filtered value
$\overline{A}$	Reynolds averaged value

Abbreviations

DG	Discontinuous Galerkin
DNS	direct numerical simulation
FDF	filtered density function
LES	large eddy simulation
PDF	probability density function
RANS	Reynolds-averaged Navier-Stokes
SGS	subgrid scale

ACKNOWLEDGEMENTS

I would like to express my most sincere appreciation to my advisors, Drs. Peyman Givi and Shervin Sammak, without whose excellent guidance and support I would not have been able to conduct this research. I would like to thank the members of my doctoral committee, Drs. Hessameddin Babaee, Anne Robertson and Mehrdad Massoudi for their valuable suggestions on my dissertation. Also, my appreciation goes to the Graduate Program Director of Mechanical Engineering, Dr. Qing-Ming Wang for his kind advice and assistance.

I am indebted to my other colleagues at the University of Pittsburgh Laboratory for Computational Transport Phenomena (LCTP) for their cooperation and friendship: Mr. Aidyn Aitzhan, Dr. Arash Nouri Gheimassi and Mr. Krisda Tapracharoen. I wish to make special mention of my beloved friends who share hope and grow up with me; namely Ying Liao, Xue Rui, Hao Tang, Haosheng Wu, Jun Yang, Junke Zhang, Guangyi Zhao, Xingjian Zhou, Yi Zhou, Junjun Zhu and all my amazing fellows at Pitt CSSA. My deepest gratitude goes to my parents Shengying Wu and Ruxing Miao, and my brother Hongyi Miao, who provided me resources as best they can to raise and educate me, instilled the values of perseverance, modesty, and hard work in me as a youth. And last but not least, I would like to thank my dearest puppy Linghu Cong for his companionship everyday.

This work is sponsored by National Science Foundation (NSF) under Grants CBET-1609120 and CBET-1603131. Computational resources are provided by the University of Pittsburgh Center for Research Computing.

LING MIAO

UNIVERSITY OF PITTSBURGH, 2018

1.0 INTRODUCTION

Large eddy simulation (LES) is now broadly accepted as the optimal means of capturing the physics of turbulent reacting flows among the computational fluid dynamics (CFD) methodologies currently available [1–8]. In LES, there are two basic assumptions: 1. the transport of momentum, energy and passive scalars is mostly governed by the unsteady features in the larger length scales; 2. smaller scales are more universal in their behavior. Under these assumptions, LES calculates the large-scale unsteady turbulent motions, while the effects of the smaller-scale motions are solved via a so-called subgrid scale (SGS) model [9]. In doing so, the coupling between the numerical method and SGS modeling is of great importance [10].

One of the most challenging issues in LES is associated with capturing SGS fluid flow behavior. A large number of SGS models have been developed for the turbulent stress tensor [11–19]. Vreman *et al.* [20] test and compare six important representatives of the available SGS models. The dynamic models are found to generate better results than the non-dynamic models. Among different models, the filtered density function (FDF) methodology has been proven particularly effective for consistent modeling of the SGS quantities [21–27]. Essentially FDF is the counterpart of the probability density function (PDF) methodology in Reynolds-averaged Navier-Stokes (RANS) simulations [24, 27, 28]. In its most comprehensive, stand-alone form, FDF addresses the joint statistics of the following SGS variables: energy, pressure, frequency, velocity and all other scalar variables [29, 30]. Another most critical challenge in LES, or more generally in CFD, is to develop high-order accurate and stable numerical methods [31].

Both the LES filter size and the grid resolution are the most important length scales in LES. The former usually appears in the SGS models, and the latter is a critical consideration in every numerical method. Compared to DNS, LES performs a low-pass filtering operation that allows the filtered velocity field to be solved on a relatively coarse grid, thus requires less computational effort or can simulate flows at higher Reynolds numbers. In most of the past numerical works, the grid spacing is set to be proportional to the specified filter size, while it should be pointed out that these two length scales are actually independent from each other. The effects of each, however, could be examined as the ratio of the filter size to the grid size, Δ/h. A large value of Δ/h contributes to good numerical accuracy, whereas a smaller value benefits resolving more small scale turbulent motions while sacrifices more numerical accuracy [32]. This natually leads to the consideration of a optimal choice of the filter size and the grid size. Ideally the filter size should be somewhat smaller than the size of the smallest energy-containing motions, while the grid spacing is as large as possible, subject to the condition that the energy-containing motions are resolved [24]. But whether there exits an optimal value remains a question, as well as what and how other factors affect the optimal value. There have been some discussions and a point of view is that the optimal value of Δ/h varies with different approaches and SGS models being used [33, 34]. The role of the filter-grid ratio Δ/h has been examined in a few previous works both theoretically and numerically. Ghosal [35] proposes a general non-linear analysis of the numerical error in the solution of the Navier-Stokes equations for an isotropic homogeneous turbulent flow. His theoretical evaluations show that for schemes of different order of accuracy, the dominance of the subgrid term on the whole of the solution spectrum is ensured for different values of Δ/h. Chow and Moin [36] assess Gholsal's results by taking into account the nonlinear feedback of the computed solution on the numerical error. The minimum of the filter-grid ratio that can ensure the dominance of the subgrid terms is found to be a decreasing function of the scheme's order of accuracy. Geurts and Frohlich [37, 38] investigated the efficiency of the prefiltering technique on the plane mixing layer configuration. They concluded that the best solution for improving the results of a LES in practice is to refine the computational grid, while keeping a low value of the ratio Δ/h.

In this work, we use the discontinuous Galerkin (DG) method as the base flow solver for simulating unsteady turbulent flows. This method combines the ideas of finite-element and finite-volume methods to provide high-order approximations of the filtered transport equations while allowing geometric flexibility. In Refs. [39, 40], we demonstrate the capability of DG method for LES of turbulent combustion and shock capturing. DG uses a basis that is continuous within an element but discontinuous between elements, and each element can have a different polynomial degree p for the solution and the geometrical mapping. Also the basis for the solution and the geometrical mapping can be chosen independently. The advantage of the DG scheme is that it supports curved mixed-element meshes, variable discretization order, and non-conforming mesh element refinement. These features enable the flow solver to support combined $h-p$ refinement which can result in optimal solution accuracy for a given computational cost [41, 42]. Based on the close to exponential convergence of p refinement, the procedure is much more efficient than the conventional approach of refining the grid (reducing h) as is the typical practice in typical Eulerian LES.

1.1 OBJECTIVE AND SCOPE

The first objective of the present work is to implement the DG method for LES. Different cases are tested of a two-dimensional temporally developing mixing layer and the first two moments of the DG solutions are assessed. The solutions are compared with the filtered DNS data to verify the predictive capability. This is demonstrated with comparing the profiles of the subgrid, resolved and total variance for different Δ/h, and further analyzed by the error of the LES solutions as compared with the filtered DNS data. The second objective of the work is to extend the simulations to three-dimensional temporally developing mixing layer, and to examine how the filter size along with the grid size influences the LES solutions. The filter width, grid resolution and the order of spectral discretization are varied independently to assess the effects of each by comparing the first two moments of the solutions. Comparative assessments are also made via the use of high resolution DNS data.

This dissertation is organized as follows. In chapter 2, the DG solver is developed and tested for LES of a two-dimensional mixing layer. In chapter 3, the simulations are extended to a three-dimensional mixing layer. In chapter 4, some concluding remarks are provided.

2.0 TWO-DIMENSIONAL MIXING LAYER

In the work described in this chapter, a DG solver is implemented for LES and tested on a two-dimensional temporally developing mixing layer. Some systematic analysis will be performed by changing the grid and filter size, as well as polynomial degree, and comparing the LES solutions with the filtered DNS data.

2.1 FORMULATION

The mathematical formulation starts with the governing equations of a two-dimensional non-reactive, low-speed variable density flow carrying a passive scalar. The primary transport variables are the density $\rho(\mathbf{x}, t)$, the velocity vector $u_i(\mathbf{x}, t)(i = 1, 2)$, the pressure $P(\mathbf{x}, t)$, and the scalar mass fractions $\phi(\mathbf{x}, t)$. The equations which govern the transport of these variables in space $(x_i)(i = 1, 2)$ and time (t) are the continuity, momentum, and conservation of mass fraction equations:

$$\frac{\partial \rho}{\partial t} + \frac{\partial \rho u_j}{\partial x_j} = 0, \tag{2.1a}$$

$$\frac{\partial \rho u_i}{\partial t} + \frac{\partial \rho u_j u_i}{\partial x_j} = -\frac{\partial P}{\partial x_i} + \frac{\partial T_{ji}}{\partial x_j}, \tag{2.1b}$$

$$\frac{\partial \rho \phi}{\partial t} + \frac{\partial \rho u_j \phi}{\partial x_j} = -\frac{\partial J_j}{\partial x_j}. \tag{2.1c}$$

These equations are coupled with an appropriate equation of state. For a Newtonian fluid, the most widely used Fourier's law of heat conduction and Fick's law of diffusion define the viscous stress tensor T_{ij} and the scalar flux J_j by

$$T_{ij} = \mu \left(\frac{\partial u_i}{\partial x_j} + \frac{\partial u_j}{\partial x_i} - \frac{2}{3} \frac{\partial u_k}{\partial x_k} \delta_{ij} \right), \; J_j = -\gamma \frac{\partial \phi}{\partial x_j}, \tag{2.2}$$

where μ is the fluid dynamic viscosity, $\gamma = \mu / Sc$ denotes the mass molecular diffusivity coefficient, and Sc is the Schmidt number. Both μ and γ are assumed constant and Schmidt number is assumed to be unity.

Large eddy simulation involves the spatial filtering operation [24, 43]. Such filtering operation can be either implicit or explicit. For implicit filtering, the numerical grid itself is assumed to be the LES low-pass filter. This operation takes full advantages of the numerical grid resolution and eliminates the computational cost of calculating a subfilter scale model term. But it is also difficult to determine the shape of the LES filter that can be useful for some numerical methods. The trucation error can also be an issue [44]. The advantages of explicit filtering operation, however, are that the filter shape is well defined and truncation error can be reduced. While on the other hand, it faces the problem of loss of resolution. The space resolution has to be fine enough in order to correctly integrate the convolution product that defines the analytical filtering [45]. For explicit filtering, an LES filter is applied to the numerical grid, *i.e.*, explicitly to the discretized Navier-Stokes equations. Mathematically, we have

$$\langle Q(\mathbf{x}, t) \rangle_\ell = \int_{-\infty}^{+\infty} Q(\mathbf{x}', t) G(\mathbf{x}', \mathbf{x}) \; \mathrm{d}\mathbf{x}', \tag{2.3}$$

where $G(\mathbf{x}', \mathbf{x}) \equiv G(\mathbf{x}' - \mathbf{x})$ denotes a filter function, and $\langle Q(\mathbf{x}, t) \rangle_\ell$ is the filtered value of the transport variable $Q(\mathbf{x}, t)$. In variable-density flows it is convenient to use the Favré-filtered quantity $\langle Q(\mathbf{x}, t) \rangle_L = \langle \rho Q \rangle_\ell / \langle \rho \rangle_\ell$. We apply the filtering operation with a filter function that is spatially varying, to Eq. (2.1):

$$\frac{\partial \langle \rho \rangle_\ell}{\partial t} + \frac{\partial \langle \rho \rangle_\ell \langle u_j \rangle_L}{\partial x_j} = 0, \tag{2.4}$$

$$\frac{\partial \langle \rho \rangle_\ell \langle u_i \rangle_L}{\partial t} + \frac{\partial \langle \rho \rangle_\ell \langle u_j \rangle_L \langle u_i \rangle_L}{\partial x_j} = -\frac{\partial \langle P \rangle_\ell}{\partial x_i} + \frac{\partial \langle T_{ij} \rangle_\ell}{\partial x_j} - \frac{\partial \Sigma_{ij}}{\partial x_j}, \tag{2.5}$$

$$\frac{\partial \langle \rho \rangle_\ell \langle \phi \rangle_L}{\partial t} + \frac{\partial \langle \rho \rangle_\ell \langle \phi \rangle_L \langle u_i \rangle_L}{\partial x_j} = \frac{\partial}{\partial x_j} \left(\langle \gamma \frac{\partial \phi}{\partial x_j} \rangle_\ell \right) - \frac{\partial M_j}{\partial x_j}, \tag{2.6}$$

where $\Sigma_{ij} = \langle\rho\rangle_\ell(\langle u_i u_j\rangle_L - \langle u_i\rangle_L\langle u_j\rangle_L)$ and $M_j = \langle\rho\rangle_\ell(\langle u_j\phi\rangle_L - \langle u_j\rangle_L\langle\phi\rangle_L)$ denote the SGS stresses and the subgrid mass fluxes respectively. For the closure problem, we employ the standard Smagorinsky model [46, 47]:

$$\Sigma_{ij} - \frac{2}{3}\langle\rho\rangle_\ell C_{\nu_2}\Delta^2 S^2\delta_{ij} = -2\mu_t\left(\langle S_{ij}\rangle_L - \frac{1}{3}\langle S_{kk}\rangle_L\delta_{ij}\right),$$
$$M_j = -\gamma_t\frac{\partial\langle\phi\rangle_L}{\partial x_j}. \tag{2.7}$$

$\langle S_{ij}\rangle_L$ is the filtered strain rate tensor given by:

$$\langle S_{ij}\rangle_L = \frac{1}{2}\left[\frac{\partial\langle u_i\rangle_L}{\partial x_j} + \frac{\partial\langle u_j\rangle_L}{\partial x_i}\right]. \tag{2.8}$$

The SGS viscosity is modeled by $\mu_t = \langle\rho\rangle_\ell[C_{\nu_1}\Delta]^2 S$, where $C_{\nu_1} = 0.17$, $C_{\nu_2} = 0.18$, $\gamma_t = \mu_t/Sc_t$, $Sc_t = 1$, $S = \sqrt{2\langle S_{ij}\rangle_L\langle S_{ij}\rangle_L}$.

We consider the filtered density function (FDF) which contains the complete SGS statistical information of the scalars, denoted by:

$$F_L(\boldsymbol{\psi}, \mathbf{x}, t) = \int_{-\infty}^{+\infty}\rho(\mathbf{x}', t)\zeta(\boldsymbol{\psi}, \boldsymbol{\phi}(\mathbf{x}', t))G(\mathbf{x}' - \mathbf{x})\ \mathrm{d}\mathbf{x}', \tag{2.9}$$

where

$$\zeta(\boldsymbol{\psi}, \boldsymbol{\phi}(\mathbf{x}, t)) = \delta(\psi - \phi(\mathbf{x}, t)). \tag{2.10}$$

Here, δ denotes the Dirac delta function, and $\boldsymbol{\psi}$ represents the scalar array in the sample space. The term ζ is the "fine-grained" density [48, 49]. Equation (2.9) defines FDF as the spatially filtered value of the fine-grained density. With the condition of a positive filter kernel [50], F_L has all the properties of a mass density function [49]. Defining the "conditional filtered value" of $Q(\mathbf{x}, t)$ as:

$$\langle Q \mid \boldsymbol{\psi}\rangle_\ell \equiv \frac{\int_{-\infty}^{+\infty} Q(\mathbf{x}', t)\rho(\mathbf{x}', t)\zeta(\boldsymbol{\psi}, \boldsymbol{\phi}(\mathbf{x}', t))G(\mathbf{x}' - \mathbf{x})\ \mathrm{d}\mathbf{x}'}{F_L(\boldsymbol{\psi}, \mathbf{x}, t)}, \tag{2.11}$$

the FDF is governed by the exact transport eqution [10]:

$$\frac{\partial F_L}{\partial t} + \frac{\partial\left[\langle u_j(\mathbf{x}, t) \mid \boldsymbol{\psi}\rangle_\ell F_L\right]}{\partial x_j} = \frac{\partial}{\partial\psi}\left[\left\langle\frac{1}{\rho(\boldsymbol{\phi})}\frac{\partial J_j}{\partial x_j}\middle|\boldsymbol{\psi}\right\rangle_\ell F_L\right]. \tag{2.12}$$

This is an exact transport equation for the FDF. The first term on the right-hand side is due to the effect of chemical reaction and is in a closed form. The unclosed nature of SGS

convection and mixing is exhibited via the conditional filtered values in the other two terms. For closure of these terms, a gradient diffusion model is considered for convection, and the linear mean square estimation (LMSE) [51, 52] for molecular mixing, given by the system of stochastic differential equations (SDEs) [24, 48]:

$$\mathrm{d}x_i^+(t) = \left[\langle u_i\rangle_L + \frac{1}{\langle\rho\rangle_\ell}\frac{\partial(\gamma+\gamma_t)}{\partial x_i}\right]\,\mathrm{d}t + \sqrt{2(\gamma+\gamma_t)/\langle\rho\rangle_\ell}\;\mathrm{d}W_i(t), \tag{2.13}$$

$$\mathrm{d}\phi^+ = -\Omega_m(\phi^+ - \langle\phi\rangle_L)\;\mathrm{d}t. \tag{2.14}$$

where $\mathrm{d}W_i$ is the Wiener-Levy process [53] and, x_i^+ and ϕ^+ are probabilistic representations of the position and the scalar variables, respectively. In the model, $\Omega_m = C_\phi(\gamma+\gamma_t)/\left(\langle\rho\rangle_\ell\Delta^2\right)$ is the SGS mixing frequency and $C_\phi = 4$ is a model constant. In statistical mechanics, the Fokker-Planck equation (also known as the Kolmogorov forward equation) is a partial differential equation that describes Brownian motion. The Fokker-Planck equation corresponding to this model is (detailed derivation see [54]):

$$\begin{aligned}\frac{\partial F_L}{\partial t} + \frac{\partial\left[\langle u_j\rangle_L F_L\right]}{\partial x_j} &= \frac{\partial}{\partial x_j}\left[(\gamma+\gamma_t)\frac{\partial(F_L/\langle\rho\rangle_\ell)}{\partial x_j}\right] \\ &\quad + \frac{\partial}{\partial\psi}[\Omega_m(\psi - \langle\phi\rangle_L)F_L].\end{aligned} \tag{2.15}$$

Equation (2.15) represents the modeled FDF transport equation. The generalized first SGS moment $\langle\phi\rangle_L$ and the SGS variance $\tau \equiv \tau(\phi,\phi)$ are mostly considered for our study. These moments are obtained via integration of the modeled FDF transport equation (Eq. (2.15)), given by:

$$\frac{\partial(\langle\rho\rangle_\ell\langle\phi\rangle_L)}{\partial t} + \frac{[\langle\rho\rangle_\ell\langle u_j\rangle_L\langle\phi\rangle_L]}{\partial x_j} = \frac{\partial}{\partial x_j}\left[(\gamma+\gamma_t)\frac{\partial(\langle\phi\rangle_L)}{\partial x_j}\right], \tag{2.16}$$

$$\begin{aligned}\frac{\partial(\langle\rho\rangle_\ell\tau)}{\partial t} + \frac{[\langle\rho\rangle_\ell\langle u_j\rangle_L\tau]}{\partial x_j} &= \frac{\partial}{\partial x_j}\left[(\gamma+\gamma_t)\frac{\partial\tau}{\partial x_j}\right] + 2(\gamma+\gamma_t)\left[\frac{\partial(\langle\phi\rangle_L)}{\partial x_j}\frac{\partial(\langle\phi\rangle_L)}{\partial x_j}\right] \\ &\quad - 2\Omega_m\langle\rho\rangle_\ell\tau.\end{aligned} \tag{2.17}$$

These equations are identical to those which would be obtained by employing consistent closure for the SGS fluxes and the disspiation from Eq. (2.6).

The parameter Δ denotes the characteristic filter size. In the following study, it will be varied for different values of the ratio Δ/h. The above formulations also serve as an evidence for the fact that the effect of Δ/h varies with different SGS model, since the filtered velocity field depends on the type of filter and filter width Δ, yet these quantities do not appear directly in Eqs. (2.4)-(2.6); they appear only indirectly through the model for subgird terms. In the following study, we will focus on examining the effects of refining the resolution and changing the filter width.

2.2 DISCONTINUOUS GALERKIN SOLVER

The DG flow solver provides high-order approximations of the filtered transport equations with a flexibility to deal with complex geometries. To implement this solver, the domain is discretized into a number of structured or unstructured elements. Each of these elements are mapped from the physical space to the computational space ($\mathbf{x} \rightarrow \eta$). Within this space, the transport variable are represented via the spectral approximations. The eigenfunctions of the appropriate Sturm-Liouville problem are used for this approximation. Here the Legendre polynomials are employed in conjunction with Gauss quadrature points. In 1-D (η), these are given by:

$$\mathcal{L}_p(\eta) = \frac{1}{2^p n!}\frac{d^p}{d\eta^p}[(\eta^2-1)^p], \quad p = 0, 1, 2, \dots \ . \tag{2.18}$$

where p denotes the degree of the Legendre polynomial and η is the computational space. The number of Gauss quadrature points is given by $ngp = p + 1$. The basis functions up to order $p = 4$ are shown in Fig. 1. Detailed DG discretization and it implementation is described in APPENDIX A and Ref. [55].

The DG methodology is a combination of finite element (FE) and finite volume (FV) methodologies. The multi-element part of DG is very similar to FE but unlike FE, DG elements are disconnected at the interfaces, which makes them suitable for advection dominated problems. The problem of the lack of solution uniqueness at the interface is addressed as in FV by a numerical flux. The disconnected elements allow for flux calculation via ap-

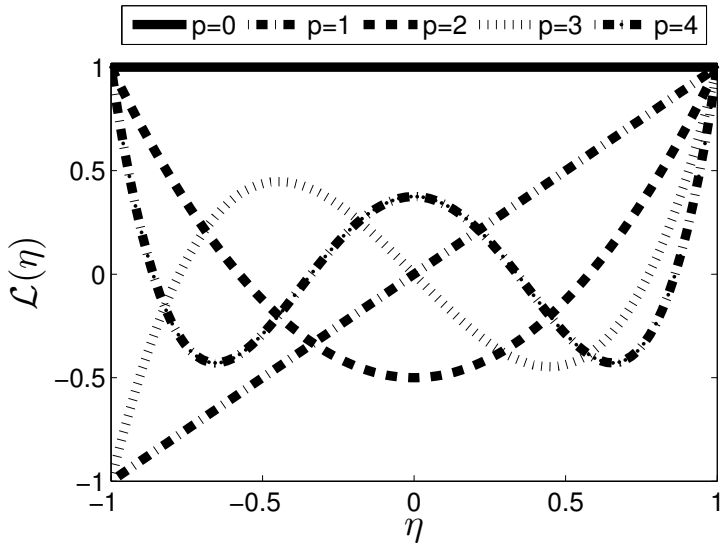

Figure 1: Basis functions for Legendre modal basis.

proximate Riemann solvers as is done here. APPENDIX B provides an error estimate test for the order of accuracy of the DG implementation [41].

The DG solver has several advantages over more conventional methods (like finite volume, finite difference and finite element). A significant advantage is that DG allows convergence to DNS limit via p-refinement. Based on the close to exponential convergence of this refinement, the procedure is much more efficient than the conventional approaches of refining the grid (reducing h) as is the typical practice. Another advantage is that the DG variables can easily be evaluated since these variables are represented by simple polynomials within each element. Hence, there is no loss of accuracy due to the use of a lower order interpolation method as is typically used in conventional approximations.

2.3 DEMONSTRATION

Large eddy simulations as well as DNS are conducted on a cube box but suppressing the third dimension as a simplified test case: $0 \leq x \leq L$, $-L/2 \leq y \leq L/2$. The length L is specified such that $L = 2^{n_p}\lambda_u$, where n_p is the desired number of succesive vortex pairings and λ_u is the wavelength of the most unstable mode corresponding to the mean stream-wise velocity profile imposed at the initial time. The simulations considered a two-dimensional, temporally developing mixing layer. Quite a number of direct numerical simulation work of such turbulent mixling layer have been reported in literature. Incompressilbe simulations have been reported by Comte *et al.* [56] and Rogers & Moser [57]. The former has shown that a periodic mixing layer developing from a hyperbolic-tangent velocity profile is subject to a violent three-dimensional instability. The latter investigated the influences of the two-dimensional disturbances of varying strength on the self-similarity. The highly compressible simulations at convective Mach number 0.2 to 1.2 are also investigated by Luo & Sandham [58] and Vreman *et al.* [59]. They have found that the flow undergoes a transition with primary instability alone, in the absence of secondary instability, vortex pairing or background noise, and the dilatational contribution to dissipation is negligible. In this work, the flow is regarded as imcompressible. Initially the layer consists of two parallel streams traveling in opposite directions with the same speed. x and y denote the stream-wise and the cross-stream flow directions respectively. The velocity components in each direction are u and v. The filtered stream-wise velocity is initialized with a hyperbolic tangent profile with $\langle u \rangle_L = 1$ on the top stream and $\langle u \rangle_L = -1$ on the bottom stream.

The flow variables are normalized with respect to $L_r = \delta_v|_{t=0}/2$, $U_r = \Delta U/2$, where $\delta_v = \Delta U/|\partial\overline{\langle u \rangle}/\partial y|_{max}$ is the initial vorticity thickness; $\overline{\langle u \rangle}$ is the Reynolds averaged value of the filtered stream-wise velocity; ΔU is the velocity difference across the layer. All of the Reynolds-averaged values are time-dependent and are determined by the ensemble averaging over the homogeneous x axis, denoted by an overbar. The Reynolds number based on L_r and U_r is $Re = 100$. The formation of the large scale vortical structures are expedited by harmonic forcing of the layer. This results in the formation of n_p successive vortex pairings.

Both DNS and LES simulations are provided by the DG solver. Temporal integration in the DG calculation is integrated via a 4th order Runge Kutta method [60]. The computational domain is discretized on euqally spaced quadrature points. Simulations are conducted on a structured hexahedral mesh. For all cases, $\langle\phi\rangle_L$ is initialized based on a hyperbolic tangent profile. Specifically, $\langle\phi\rangle_L|_{t=0} = 0.5\tanh(y) + 0.5$. 2D DNS are conducted with a mesh size $h_{DNS} = 1/32L$ and polynomial degree $p = 5$. LES simulations are conducted on different cases varing mesh size h_{LES} and filter width Δ. Analysis of the simulated results are perfromed both instantaneously and statistically. In the former, the snap-shot contours of the scalar variable are displayed. In the latter, the Reynolds averaged values are considered: the SGS stresses $\tau(a,b)$, the resolved stresses $R(a,b)$ and the total stresses $r(a,b)$,

$$\tau(a,b) = \langle ab\rangle_L - \langle a\rangle_L\langle b\rangle_L. \tag{2.19}$$

$$R(a,b) = \overline{\langle a\rangle_L\langle b\rangle_L} - \left(\overline{\langle a\rangle_L}\right)\left(\overline{\langle b\rangle_L}\right), \tag{2.20}$$

$$r(a,b) = \overline{ab} - \bar{a}\bar{b}. \tag{2.21}$$

Note that for a generic filter, $r(a,b) = R(a,b) + \overline{\tau(a,b)}$.

First the effect of varying the filter width with fixed grid resolution is examined. For simplicity, the mesh size in LES is first set to be $h_{LES} = (1/16)L$, while the DNS resolution $h_{DNS} = (1/128)L$. Then the filter size $\Delta = C * h_{LES}$ takes various values with $C = 0.25, 0.5, 1, 1.5, 2$. Figure 15 shows the instantaneous contour plots of filtered scalar $\langle\phi\rangle_L$ field as computed via DNS (Fig. 2(a)) and LES (Figs. 2(b)-2(f)). These contour plots provides a visual demonstration of how the LES cases bahave compared to the DNS results, which is treated as an analytic solution here. Obviously, when the ratio Δ/h is relatively small, the number of noises in the contour plots is quite noticeable, though the grid resolution remains the same. As this ratio increases, the computational noise is decreased, but more small scale structures in the vortex are resolved. When the ratio is as high as 4, the vortex become quite small and we can easily deduct that if the ratio goes even higher, important turbulent features will hardly be observed.

The above observations for varying Δ while fixing h also lead to the question that how different grid resolution influences the solution, especially how the influence is related to

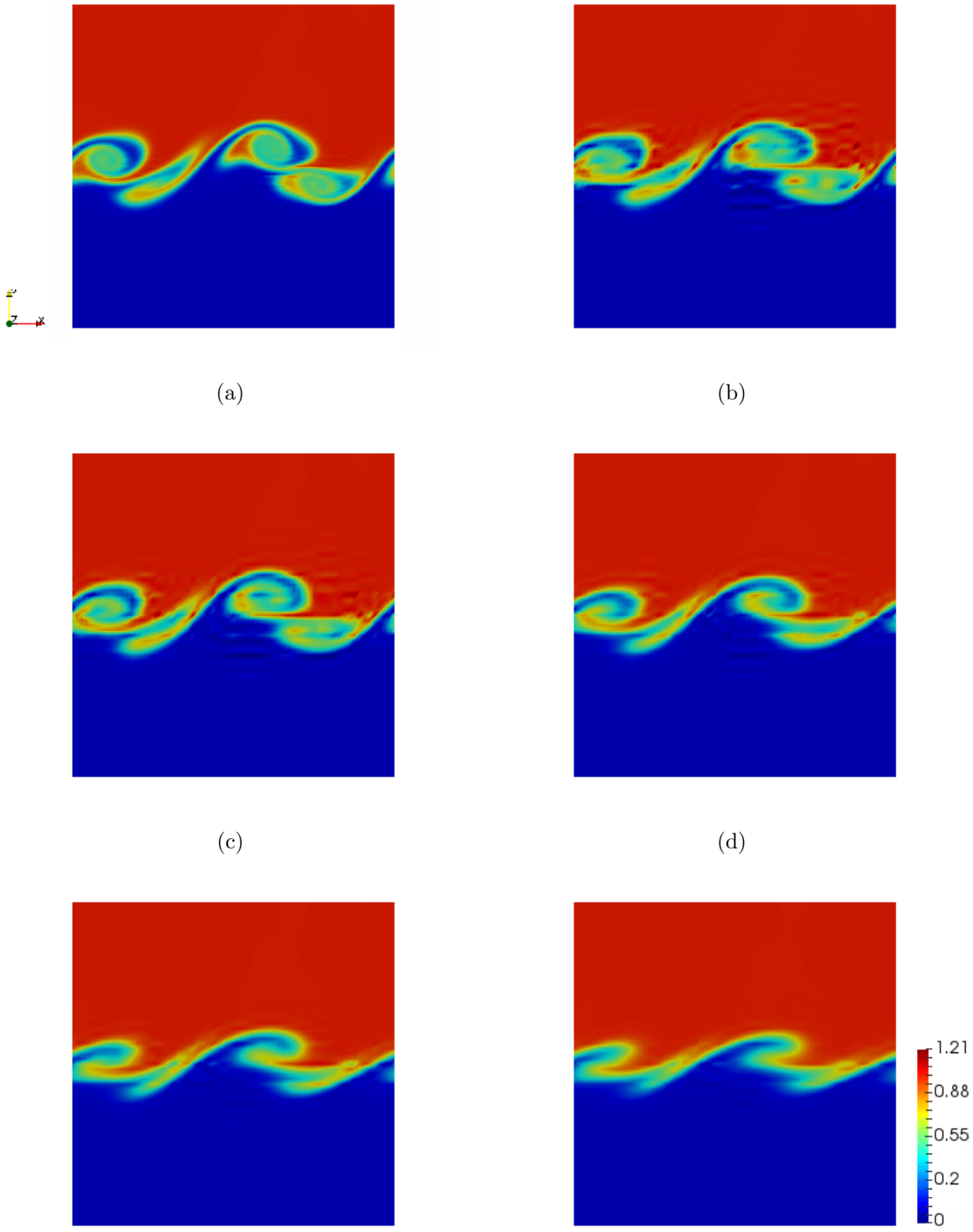

(a) (b)

(c) (d)

(e) (f)

Figure 2: Contour plots of the filtered scalar field at t=2 (a) DNS results, (b) $\Delta = 0.25h_{LES}$, (c) $\Delta = 0.5h_{LES}$, (d) $\Delta = h_{LES}$, (e) $\Delta = 1.5h_{LES}$, (f) $\Delta = 2h_{LES}$.

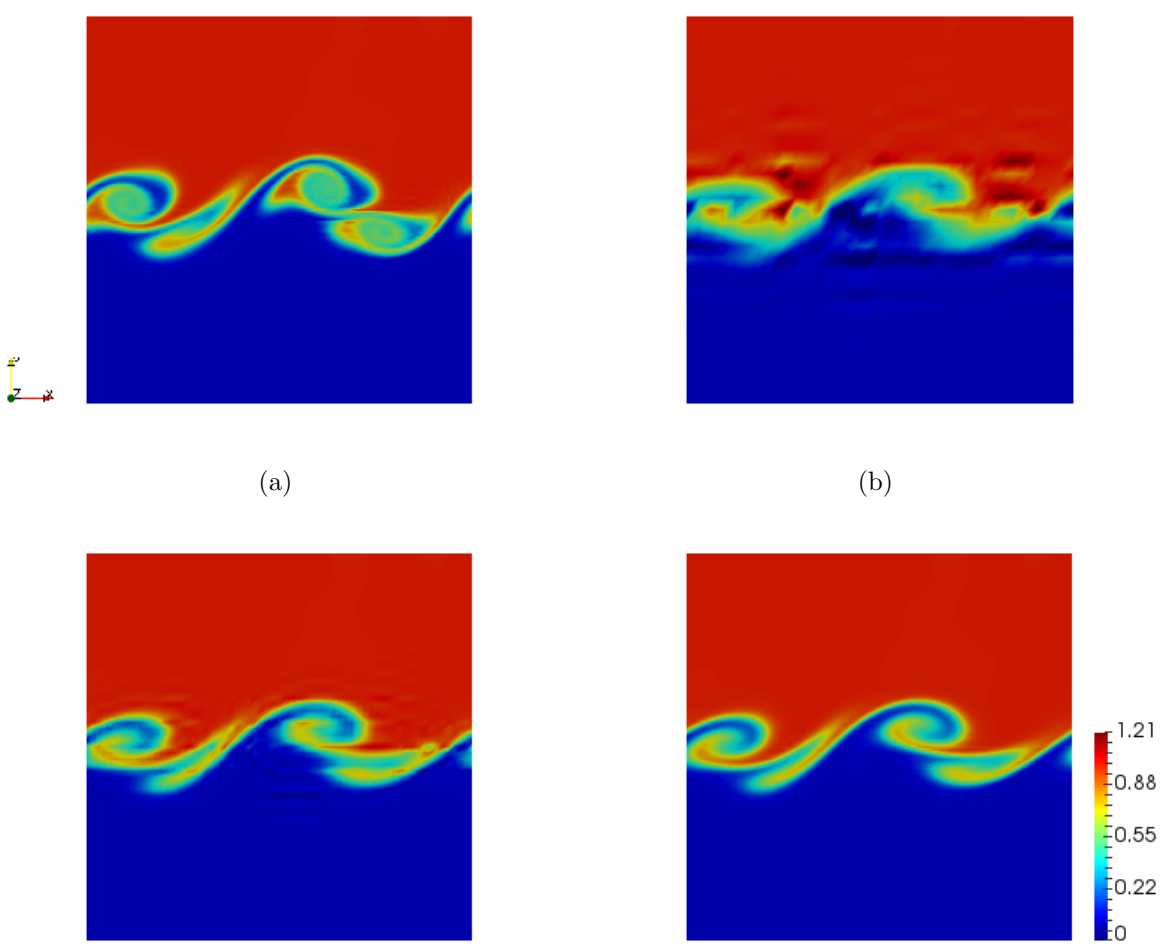

(a) (b)

(c) (d)

Figure 3: Contour plots of the filtered scalar field at $t = 2$, $\Delta = (1/16)L$ (a) DNS results, (b) $\Delta = 0.5h_{LES}$, (c) $\Delta = h_{LES}$, (d) $\Delta = 2h_{LES}$.

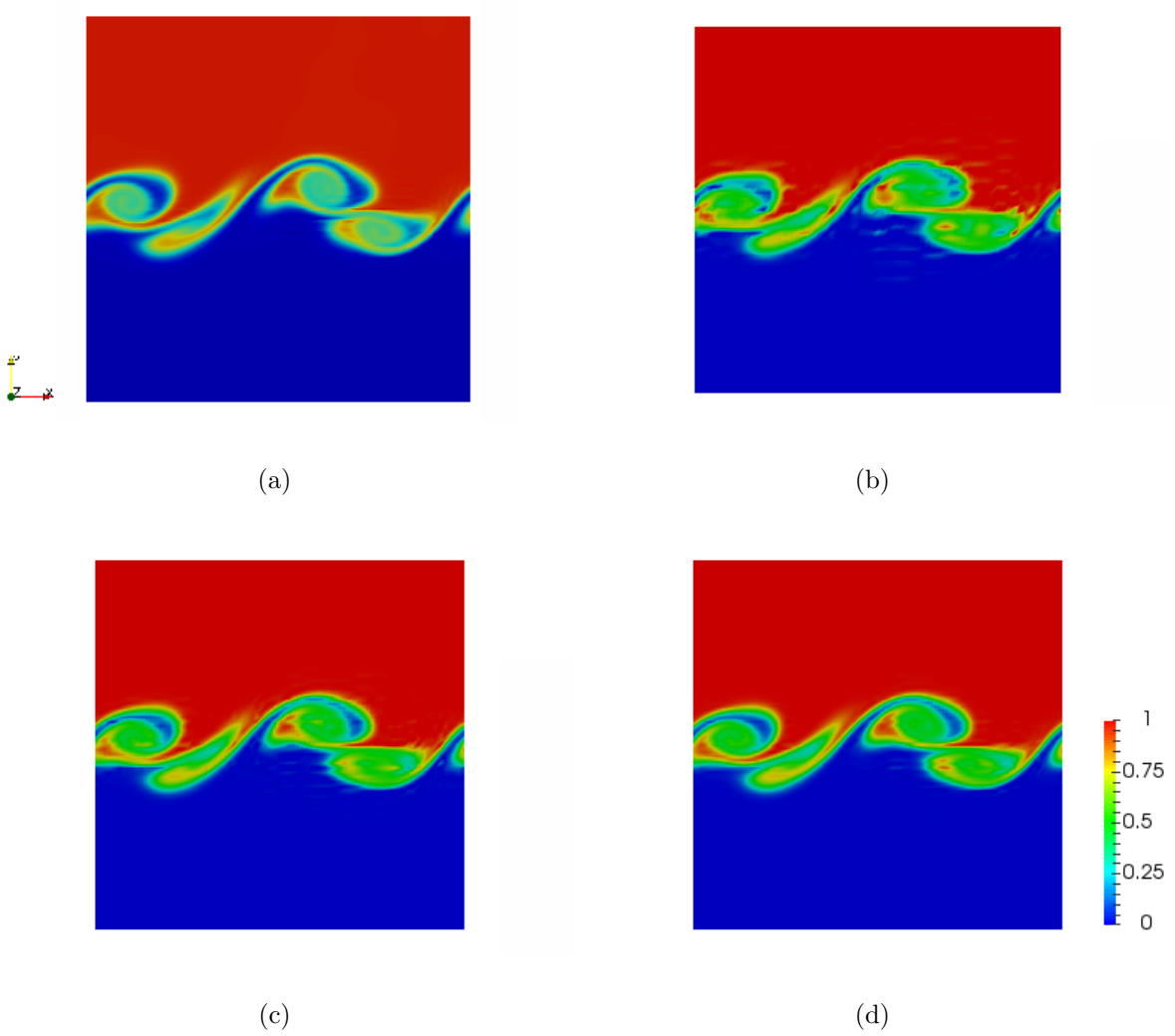

(a) (b)

(c) (d)

Figure 4: Contour plots of the filtered scalar field at t=2, $\Delta = (1/64)L, h = (1/16)L$ (a) DNS results, (b) $p = 3$, (c) $p = 4$, (d) $p = 5$.

the filter size. Figure 3 shows the instantaneous contour plots of filtered scalar $\langle\phi\rangle_L$ field of simulations with fixed $\Delta = (1/16)L$. Grid resolution in LES is refined from $h = (1/8)L$, $h = (1/16)L$, up to $h = (1/32)L$. It is obviously shown in the figures that the accuracy of the solution is improved as the grid becomes finer, but the physical behavior, *i.e.* the characteristics of the vortex pairing, is not affected. In other words, the physical characteristics is determined by the filter size Δ. Considering the simulation cost that each case consumes, the calculation with $h = (1/8)L$ took only 35 minutes wall-time, while the calculations with $h = (1/32)L$ took as much as 28 hours and 35 minutes wall-time. Compared to the cases where the grid size is fixed and filter size is varied, we can see that changing the grid size plays a more important role in affecting the overall simulation costs. From the above study, when the grid resolution is fixed, the filter size should be comparable to it in the puropose of obtaining a suffcient accuracy.

In DG-LES solver, the polymomial degree is another important parameter, as p-enrichment acts as a more efficient way to improve numerical accuracy than the conventional h-refinement. Figure 4 shows the instantaneous contour plots of filtered scalar $\langle\phi\rangle_L$ field for $p = 3, 4, 5$, and $\Delta = 1/64$ and $h = 1/16$, since in Fig. 2(b) the vortex pairing shape is the closest to the DNS result. It can be seen that when the polynomial degree is only 3, the noises in the result are quite noticeble. As we increase p up to 5, the vortex become sharp.

Figures 5-8 show the variation of several Reynolds averaged values in the cross stream as a more quantitative way of analysis. The LES resolution is now increased to be $h_{LES} = (1/64)L$ to improve the computational accuracy. Overall, for different values of Δ/h_{LES}, LES predictions are in agreement with the DNS results. The profile of the filtered scalar field is not affected much by different values of the ratio as is shown in Fig. 5. Figure 6 shows that as Δ/h_{LES} decreases, the SGS variance in LES results reduces and approaches zero, while Fig. 7 indicates no such great influence of Δ/h_{LES}. The total variance, as a result, become smaller when decreasing the ratio Δ/h_{LES}, as shown in Fig. 8.

Figures 9-12 show the influence of h_{LES} independently on the Reynolds averaged values in the cross stream direction, where $\Delta = (1/64)L$. Figure 9 indicates good agreement between all of the LES and DNS results but not much difference can be seen in the filtered scalar for

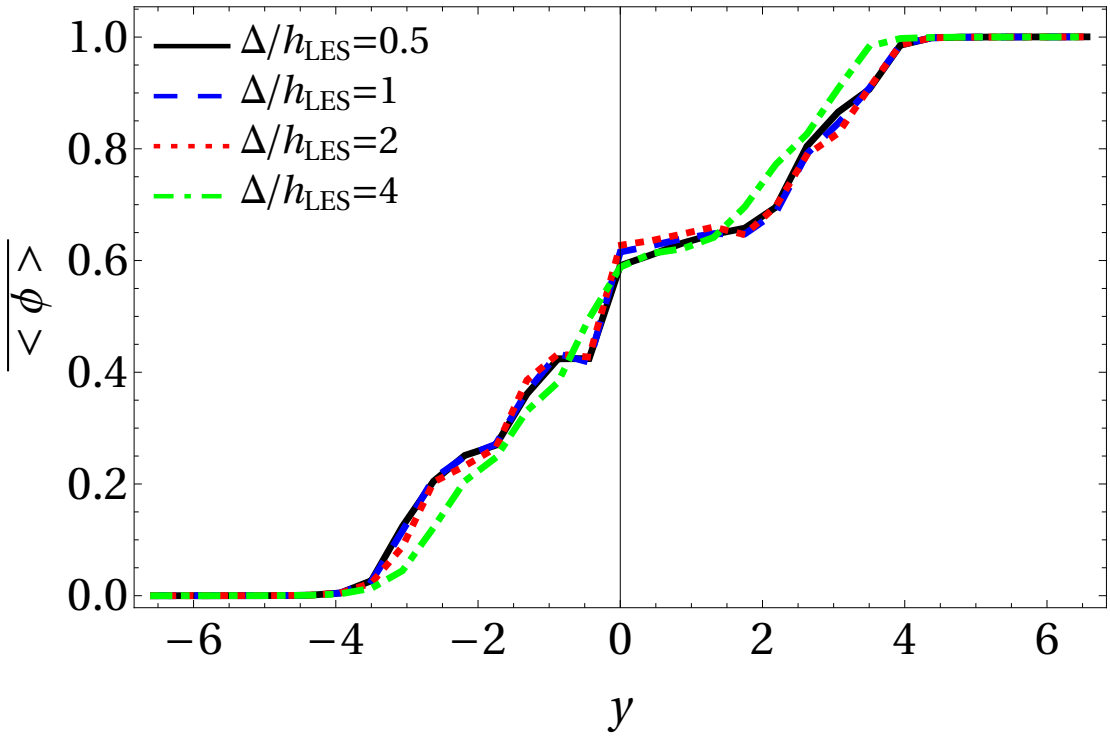

Figure 5: Cross-stream variation of the Reynolds-averaged values of the resolved scalar mean for various filter size, $p = 3, h_{LES} = (1/64)L$.

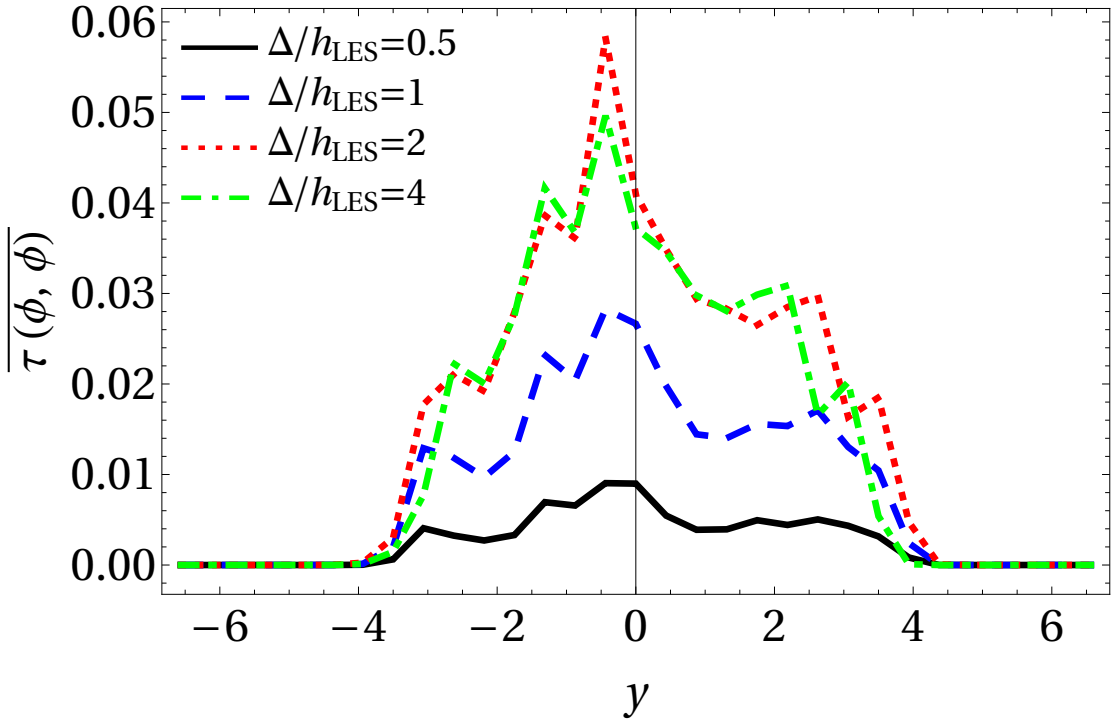

Figure 6: Cross-stream variation of the Reynolds-averaged values of SGS scalar variance for various filter size, $p = 3, h_{LES} = (1/64)L$.

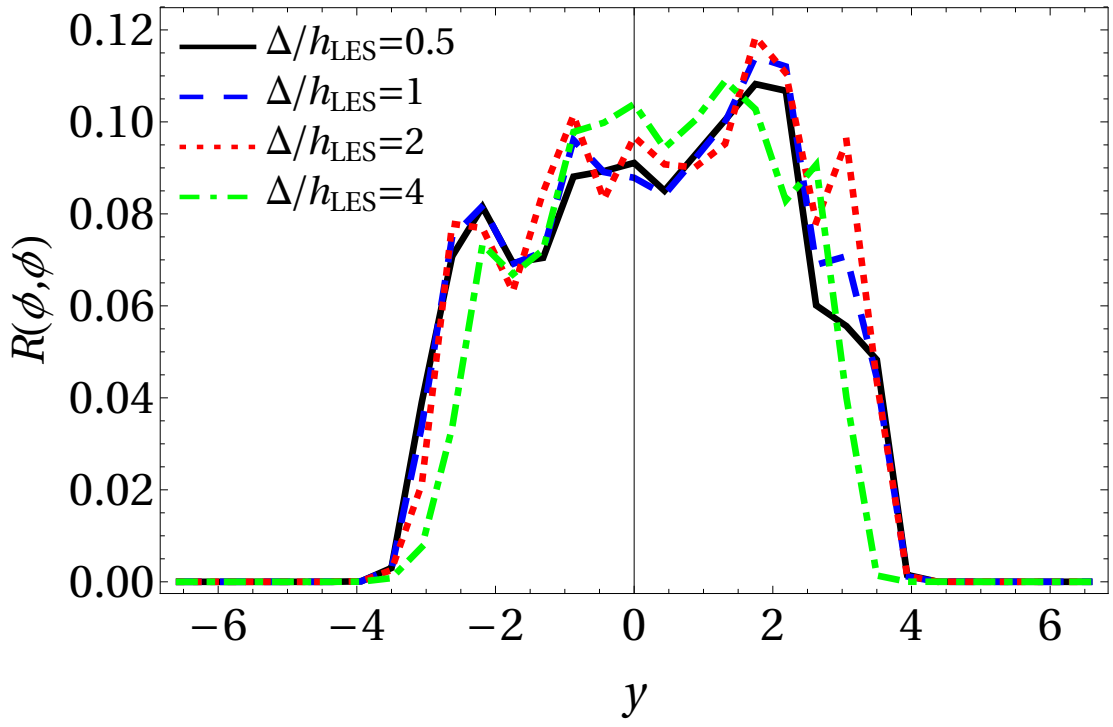

Figure 7: Cross-stream variation of the Reynolds-averaged values of resolved scalar variance for various filter size, $p = 3, h_{LES} = (1/64)L$.

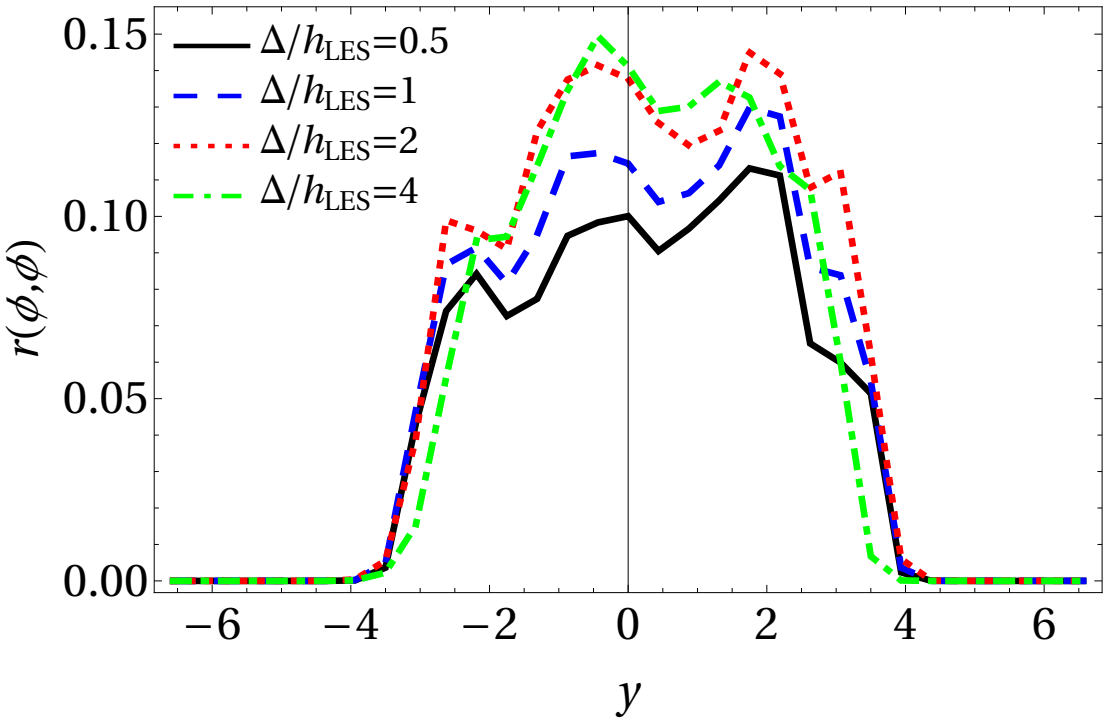

Figure 8: Cross-stream variation of the Reynolds-averaged values of total scalar variance for various filter size, $p = 3, h_{LES} = (1/64)L$.

different h. While from Figs. 11 - 12, it is shown that overall the SGS variance for different grid size stays almost the same, and is in good agreement with the filtered DNS result, but the resolved scalar variance and the total scalar variance are reduced and could converge to the DNS limit with smaller grid size. Comparing Fig. 11 and 12, about 75-80% of the scales are resovled and the rest is modeled.

To examine the influences of different filter-grid ratio values in a more systematic way, we define and calculate the error of the LES solution as compared with the filtered DNS solution. DNS results are first filtered using a simple box filter by $\langle\phi(\mathbf{x})\rangle = \int_{-\infty}^{+\infty} \phi(\mathbf{x})G(\mathbf{x}-\mathrm{r})\ \mathrm{dr}$, whose filter kernel G in physical space is given by:

$$G(\mathbf{x}-\mathrm{r}) = \begin{cases} \frac{1}{\Delta} & \text{if } |\mathbf{x}-\mathrm{r}| \leq \frac{\Delta}{2}, \\ 0 & \text{otherwise.} \end{cases} \tag{2.22}$$

The filter size Δ in this operation is determined the same as the corresponding filter width in each LES cases. The error is then calculated by

$$L_2(A) = ||A_{DNS} - A_{LES}|| = \sqrt{\frac{1}{N}\sum_{j=1}^{N}(A_{DNS_j} - A_{LES_j})^2}, \tag{2.23}$$

where N is the number of points in the y-direction, and A is any Reynolds averaged quantity of interest. The errors are plotted in Fig. 13 for different values of Δ. The results show that errors of the resolved scalar variance, SGS scalar variance and total variance achieve the minimum at smallest $\Delta = 1/128$ when $h_{LES} = (1/64)L$. Taking into account the observation in Fig. 15 when h_{LES} is only $(1/16)L$, smaller Δ gives more accurate physics but will not necessarily decrease the error since the fixed grid size becomes insufficient for relatively small filter size and the simulation will blow up at some point. It is also interesting to observe from Fig. 13 that there is a much more rapid decrease in the errors when Δ drops below $1/32$.

The L_2 norm errors of each LES simulations with different mesh sizes are also calculated and plotted in Fig. 14. By refining the mesh size, the error decreases, especially for the resolved energy and total energy. Since decreasing the filter size is an act of reducing the modeling error, while decreasing the mesh size is reducing the numerical error, varying

the filter size has a more obvious influence on the error reduction of SGS energy. The differences in the shapes prove that the filter size and grid size have independent effects on the simulation.

It is already known that in explicit filtering LES, the computational cost is roughly proportional to $(h/\Delta)^{-4}$ with a fixed filter width Δ, since the time step and number of nodes in each direction scale as h^{-1} [32]. Good resolution therefore comes at a high price: for example, doubling the resolution should increase the cost by a factor of 16. Recall that the model of SGS viscosity we used is: $\mu_t = \langle\rho\rangle_\ell [C_{\nu_1}\Delta]^2 S$, the filter size Δ acts as the similar role as the Smagorinsky constant C_{ν_1}. Therefore, when the filter size is increased, the SGS viscosity also becomes larger. Then the time spacing Δt for temporal integration has to be adjusted in order to ensure accuracy. Consequently, a smaller filter size could save computational time to some extent. Rigorously there is no such optimal choice of the ratio Δ/h. Instead, Δ and h should be chosen wisely and separately for the purpose of reducing error and capturing physics. However, based on the current analysis for the two-dimensional mixing layer, it is confirmed that the resolution $h = 1/64$ is sufficent and the SGS model employed is capable of capturing the physics. Therefore, it is convincing to suggest keeping $\Delta \approx h$ for the purpose of obtaining optimum results.

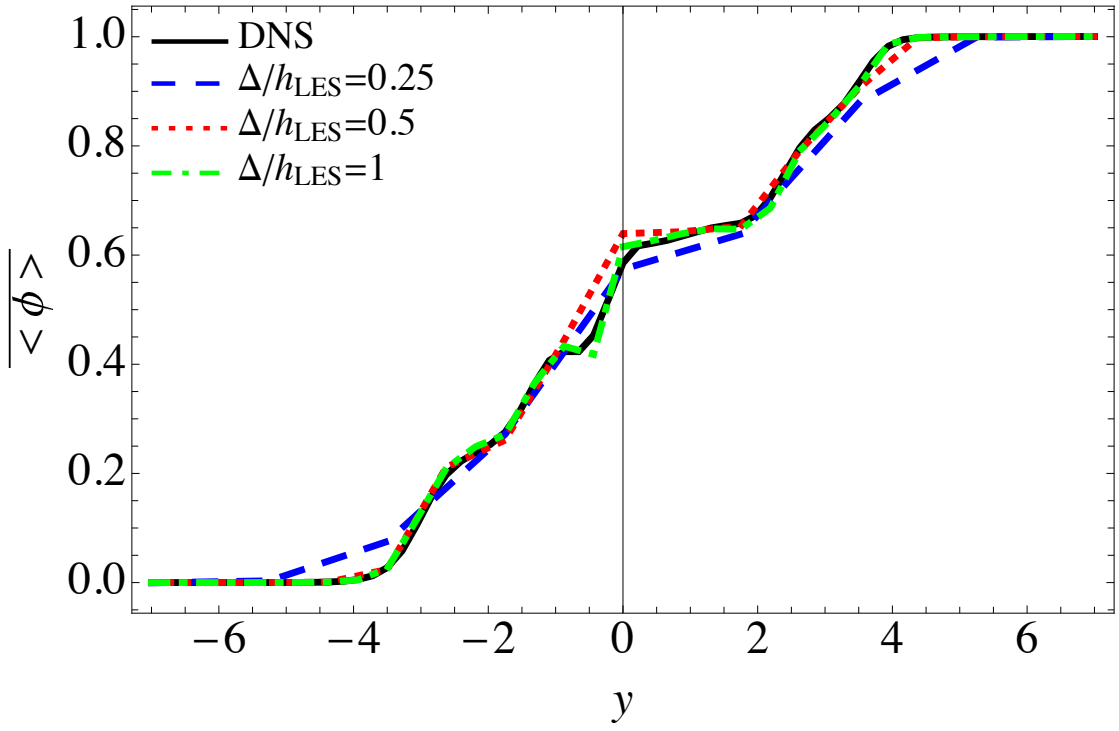

Figure 9: Cross-stream variation of the Reynolds-averaged values of resolved scalar mean for various mesh size, $\Delta = (1/64)L, p = 3$.

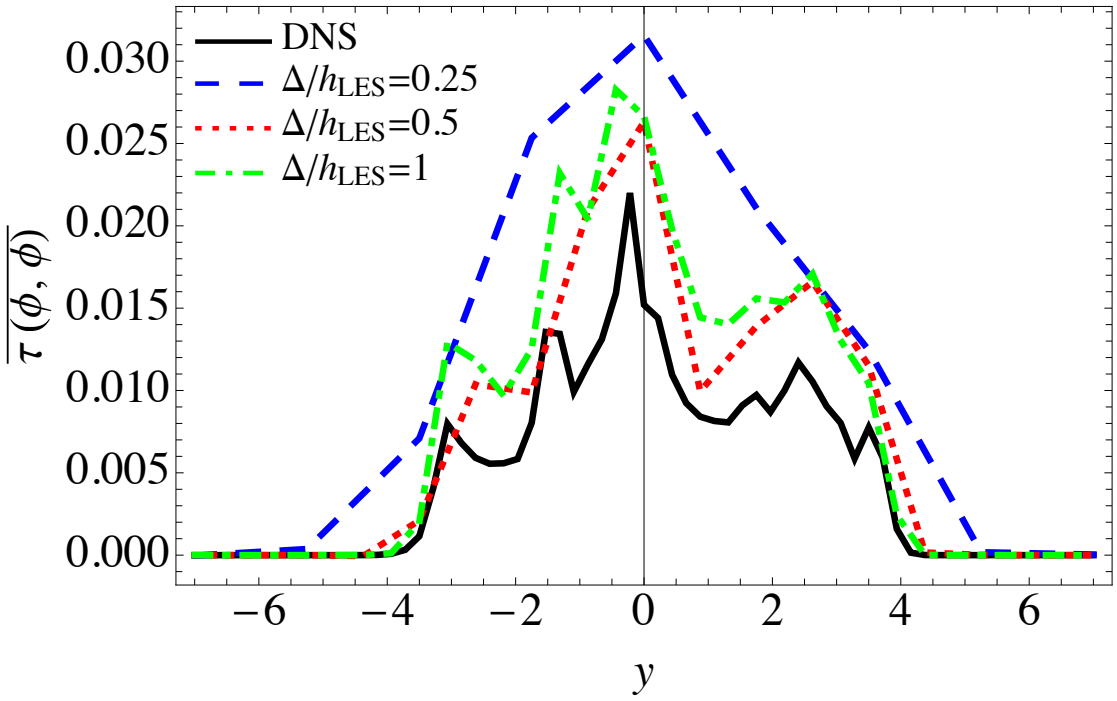

Figure 10: Cross-stream variation of the Reynolds-averaged values of SGS scalar variance for various mesh size, $\Delta = (1/64)L, p = 3$.

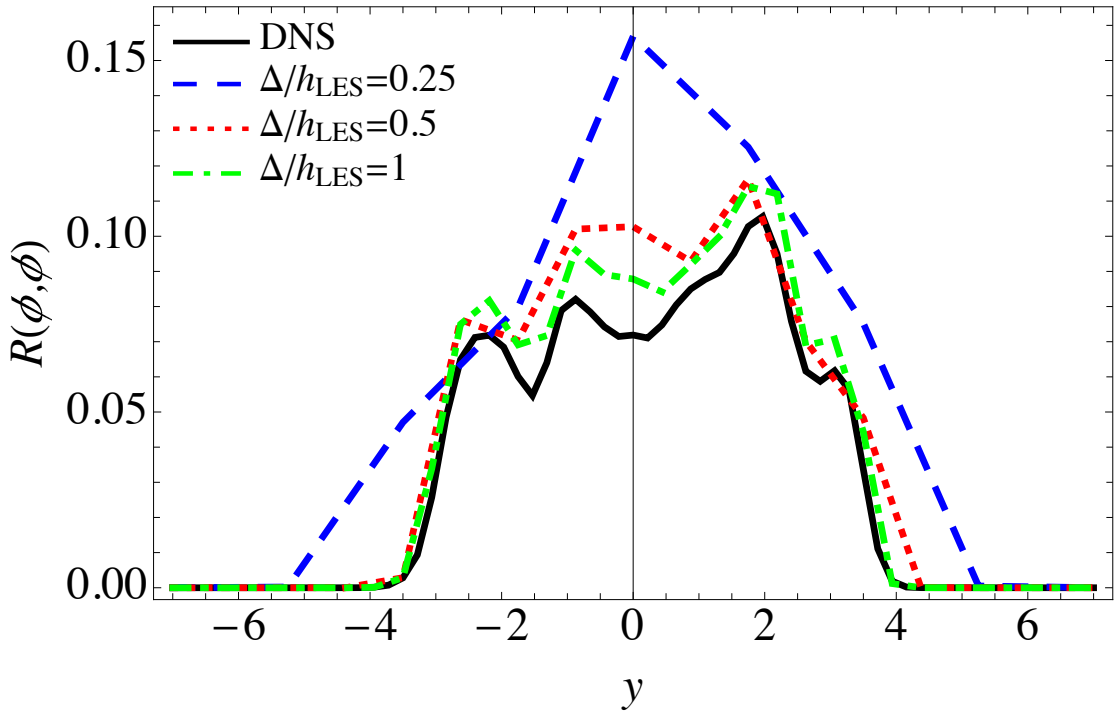

Figure 11: Cross-stream variation of the Reynolds-averaged values of resolved scalar variance for various mesh size, $\Delta = (1/64)L, p = 3$.

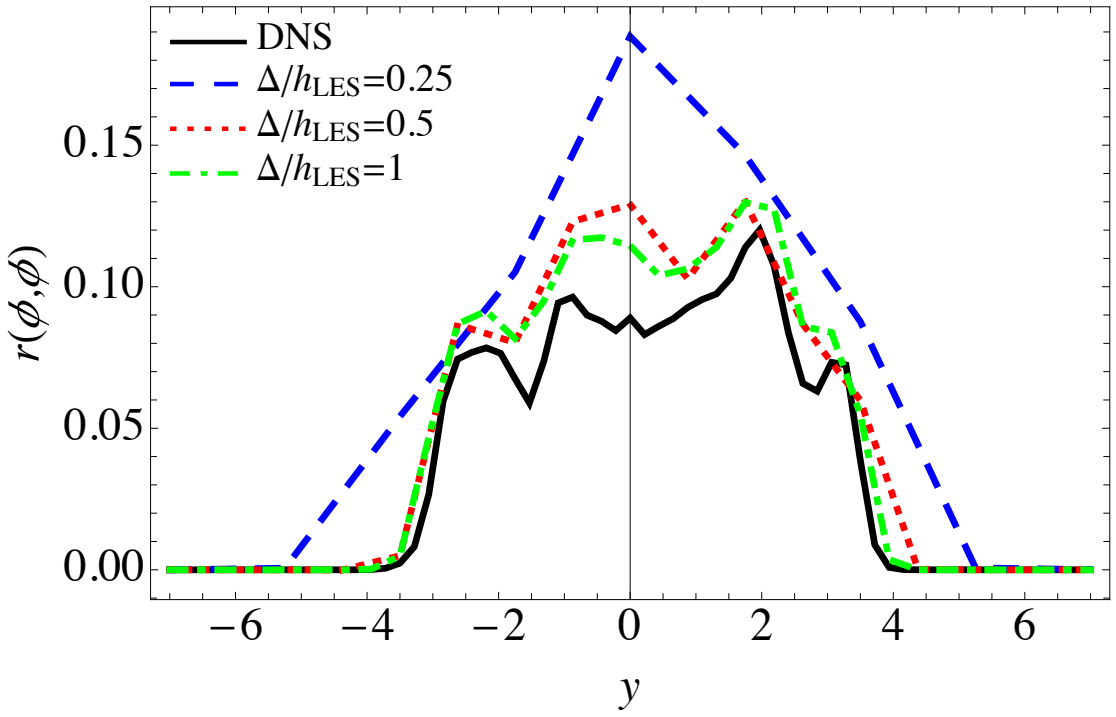

Figure 12: Cross-stream variation of the Reynolds-averaged values of total scalar variance for various mesh size, $\Delta = (1/64)L, p = 3$.

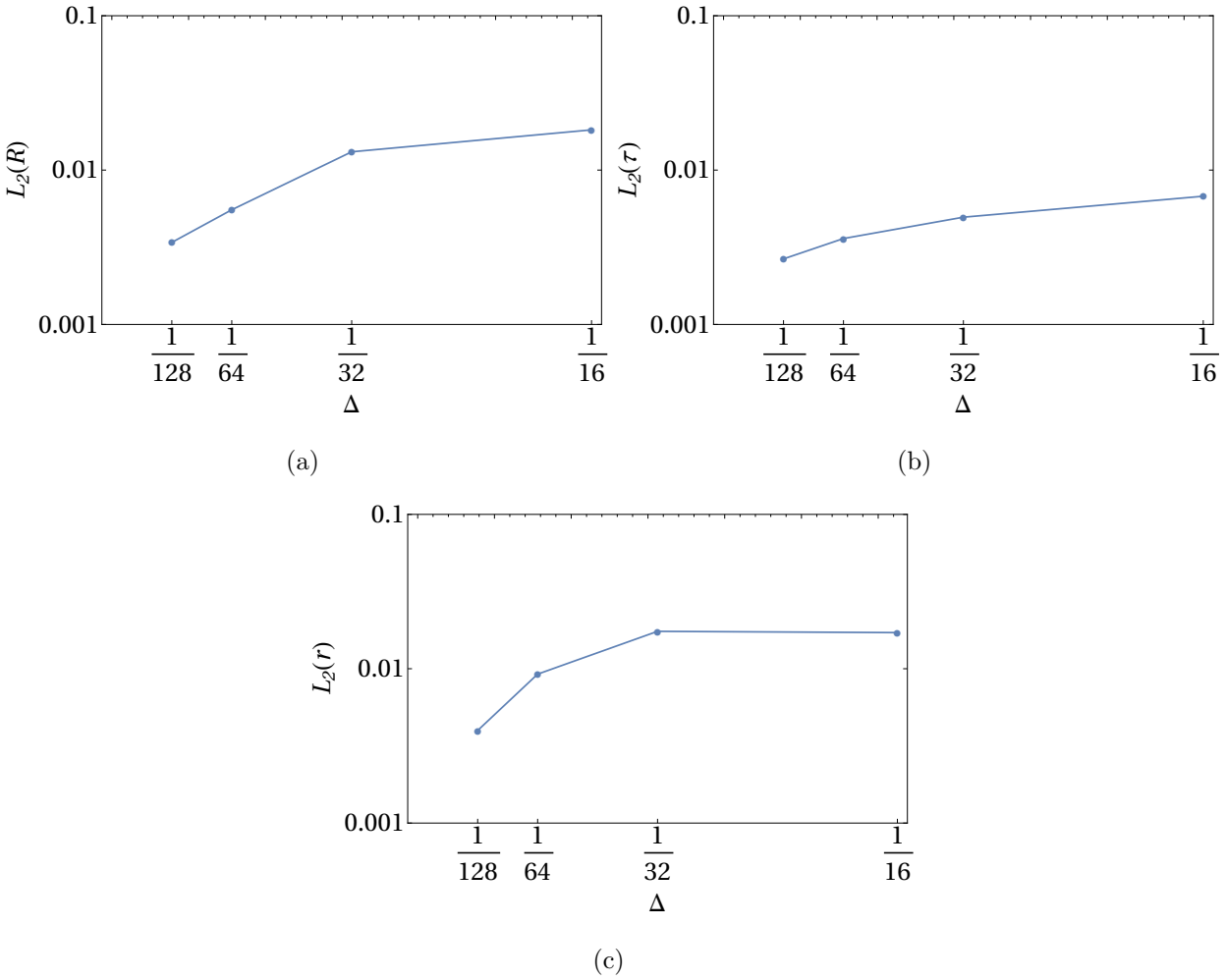

Figure 13: LES error of (a) resolved scalar variance, (b) SGS scalar variance and (c) total scalar variance, as compared with filtered DNS results for various filter size. $h_{LES} = 1/64, p = 3$.

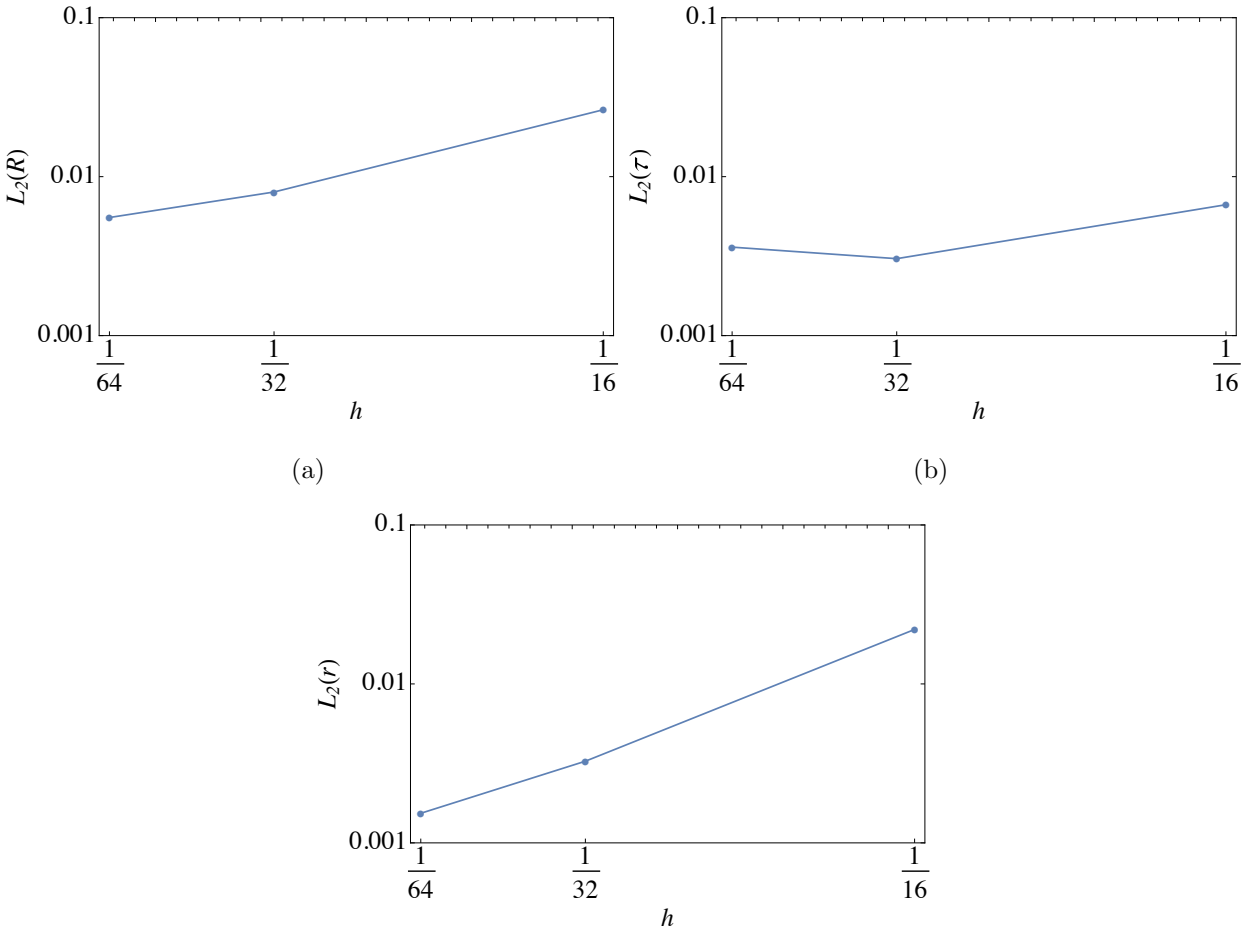

Figure 14: LES error of (a) resolved scalar variance, (b) SGS scalar variance and (c) total scalar variance, as compared with filtered DNS results for various mesh size. $\Delta = (1/64)L, p = 3$.

3.0 THREE-DIMENSIONAL MIXING LAYER

In the work described in this chapter, the DG solver is implemented for LES of a three-dimensional temporally developing mixing layer. Systematic analysis is performed by changing the grid and filter size, as well as polynomial degree; and comparing the LES predictions with the filtered DNS data.

3.1 FORMULATION

Formulation is similar to that of the two-dimensional case: the primary transport variables are the (constant) density $\rho(\mathbf{x}, t)$, the velocity vector $u_i(\mathbf{x}, t)$ $(i = 1, 2, 3)$, the pressure $p(\mathbf{x}, t)$, and the scalar mass fraction $\phi(\mathbf{x}, t)$. The equations which govern the transport of these variables in space (x_i) $(i = 1, 2, 3)$ and time (t) are the continuity, momentum and the conservation of the mass fraction equations, same as Eq. (2.1). Detailed formulation of filtering operation and filtered density function are described in chapter 2.

3.2 SIMULATIONS

For establishing the resolution criteria, extensive LES and DNS are conducted of a temporally developing mixing layer [61, 62]. In doing so, the high-order DG scheme of Sammak *et al.* [63] is used for the simulation purposes. To implement this solver, the domain is discretized

into a number of elements. Each of these elements are mapped from the physical space to the computational space ($\mathbf{x} \rightarrow \eta$). Within this space, the transport variables are represented via polynomial approximations of order p. A very significant feature of this scheme is that it allows convergence to the DNS limit via *both* $h-$ (grid size) and $p-$ refinements. Based on the close to exponential convergence of the latter, the procedure is much more efficient compared to the conventional approach of refining the grid (reducing h). The computational domain is discretized on equally spaced elements. For advective flux, Lax-Friedrichs [64], Roe [65] and artificially upstream flux vector splitting scheme [66] implemented in the DG solver. Diffusive fluxes are handled with a symmetric interior penalty method [67, 68]. Temporal integration is done via a 4th order Runge Kutta method [60].

Simulations are conducted on a cube box, $0 \leq x \leq L, -L/2 \leq y \leq L/2$ and $0 \leq z \leq L$. The box length L is specified such that $L = 2^{n_p}\lambda_u$, where n_p is the desired number of successive vortex pairings and λ_u is the wavelength of the most unstable mode corresponding to the mean stream-wise velocity profile imposed at the initial time. Here, $x,\ y$ and z denote the stream-wise, the cross-stream and the span-wise flow directions. The velocity components in these directions are denoted by $u,\ v$ and w. The filtered stream-wise velocity is initialized with a hyperbolic tangent profile with $\langle u \rangle_L = 1$ on the top stream and $\langle u \rangle_L = -1$ on the bottom stream. The flow variables are normalized with respect to $L_r = [\delta_v\,(t=0)\,/2]$ where $\delta_v = \Delta U/|\partial\overline{\langle u \rangle_L}/\partial y|_{max}$, is the initial vorticity thickness. Here $\overline{\langle u \rangle}$ is the Reynolds averaged value of the filtered stream-wise velocity and ΔU is the velocity difference across the layer. The reference velocity is $U_r = \Delta U/2$. The Reynolds number based on the reference velocity and length scales is $Re = 50$. The formation of the large scale vortical structures are expedited by harmonic forcing of the layer. This includes 2D and 3D perturbations with a random phase shift between the 3D modes [61]. This results in the formation of two successive vortex pairings and strong three dimensionality caused by the growth of secondary instabilities. In the context of the temporally developing flow, all of the Reynolds-averaged values are time-dependent and are determined by ensemble averaging over the homogeneous $x-z$ planes. In the presentation below, these are denoted by an overbar.

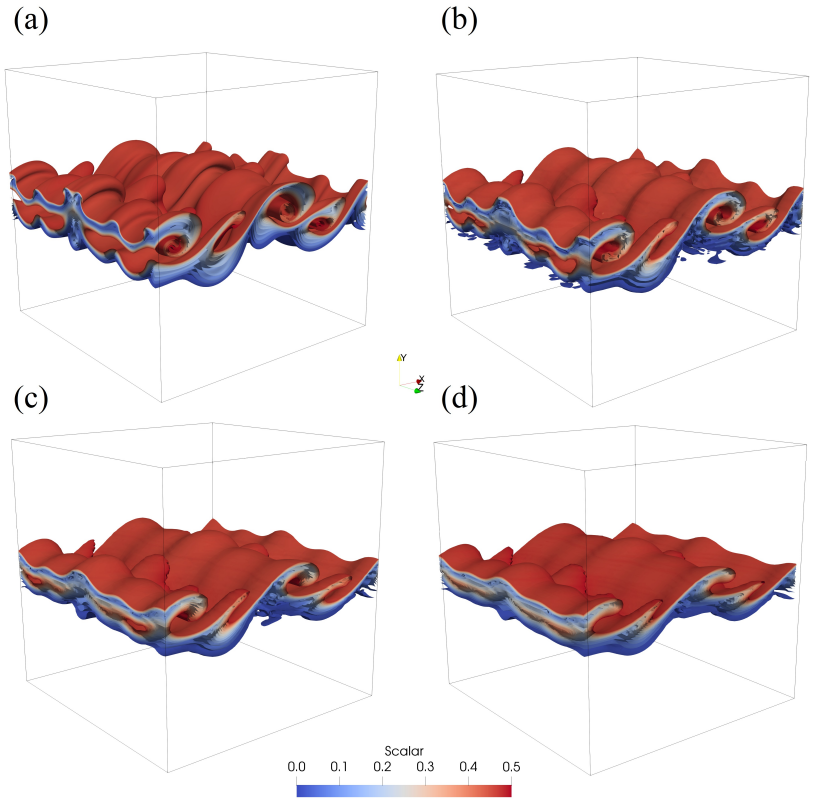

Figure 15: Contour plots of the filtered scalar field for various Δ/h sizes where $p = 4$, $h = 1/64$ and $t = 55$. (a) $\Delta/h = 0.5$, (b) $\Delta/h = 1$, (c) $\Delta/h = 2$ and (d) $\Delta/h = 4$.

3.3 DEMONSTRATIONS

The DNS simulation is conducted on a grid with $h = 1/256^3$, and $p = 5$ and LES results are investigated on a several mesh configurations with $h = 1/16^3$, $h = 1/32^3$, $1/64^3$ and $1/128^3$ and $p = 3$, $p = 4$, $p = 5$. A filter function is used with $\Delta/h = 0.5, 1, 2$ and 4. In total, 48 LES cases conducted and statistical analysis of the simulated results are performed. The Reynolds averaged values are: the SGS stresses $\tau(a,b) = \langle ab \rangle_L - \langle a \rangle_L \langle b \rangle_L$, the resolved stresses $R(a,b) = \overline{\langle a \rangle_L \langle b \rangle_L} - \left(\overline{\langle a \rangle_L}\right)\left(\overline{\langle b \rangle_L}\right)$ and the total stresses $r(a,b) = \overline{(ab)} - \overline{a}\overline{b}$.

Figure 15 shows the instantaneous contour plots of filtered scalar ($\langle \phi_\alpha \rangle_L$) field as computed for different Δ/h where $p = 4$, $h = 1/64$. This figure provides a visual demonstration of the effect of filter size, as the lower Δ/h resolves more of the total energy. This is corroborated quantitatively by the Reynolds averaged stresses presented in Fig. 16. Here, the Reynolds averaged stresses from LES results compared with filtered and unfiltered DNS as a more quantitative way of analysis. As it is presented in this figure, more than 80% of the energy is resolved. The results for the cases with other values of h, p and Δ show similar trends, and are not shown. The differences between LES and DNS results are also compared. The latter are filtered with the same width as those in LES cases, and the L_2 norm is calculated by Eq. (2.23).

Figure 17(a) indicates that for a fixed value of Δ, the SGS variance L_2 norm error decreases rapidly with larger ratio of Δ/h. While in Fig. 17(b), where h is fixed, the SGS variance L_2 norm error decreases slightly with smaller ratio of Δ/h, unlike the cases with a fixed Δ. This indicates that the increase of the grid resolution could effectively reduce the error. Moreover, the differences in Fig. 17(a) and Fig. 17(b) shows that the grid size and filter size have independent effects. It is also observed that the higher order of spectral approximation also decreases the error noticeably. Similar observations are made in Fig. 18 endorsing the above statements.

Figure 17(c) shows that as value of p increases, the amount of SGS energy decreases. This is expected and is in accord with the expectation that with increased resolution, the influence of SGS scales becomes less pronounced. This is further examined in Fig. 18(c)

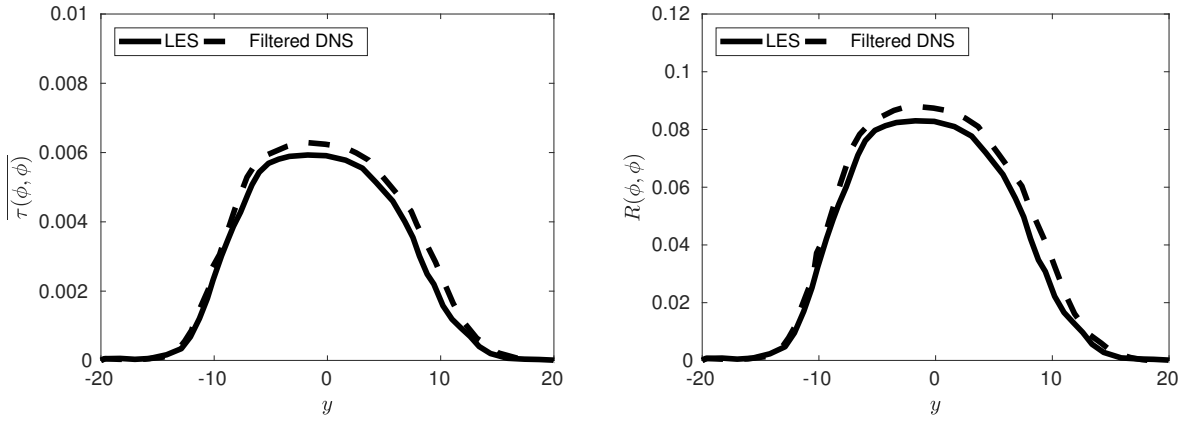

(a)

(b)

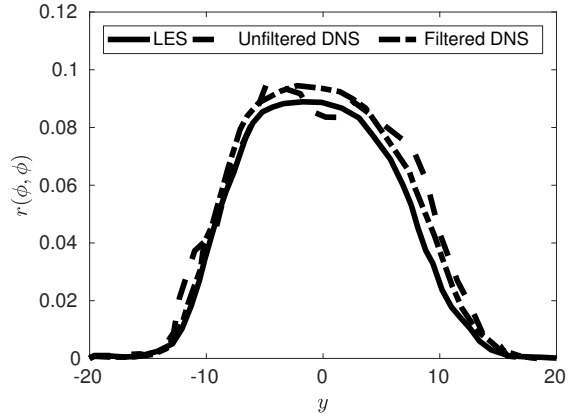

(c)

Figure 16: Cross stream variation of the Reynolds averaged values with $p = 4$, $h = 1/32$ and $\Delta = 1/32$. (a) SGS variance with, (b) resolved scalar variance with fixed, (c) total scalar variance.

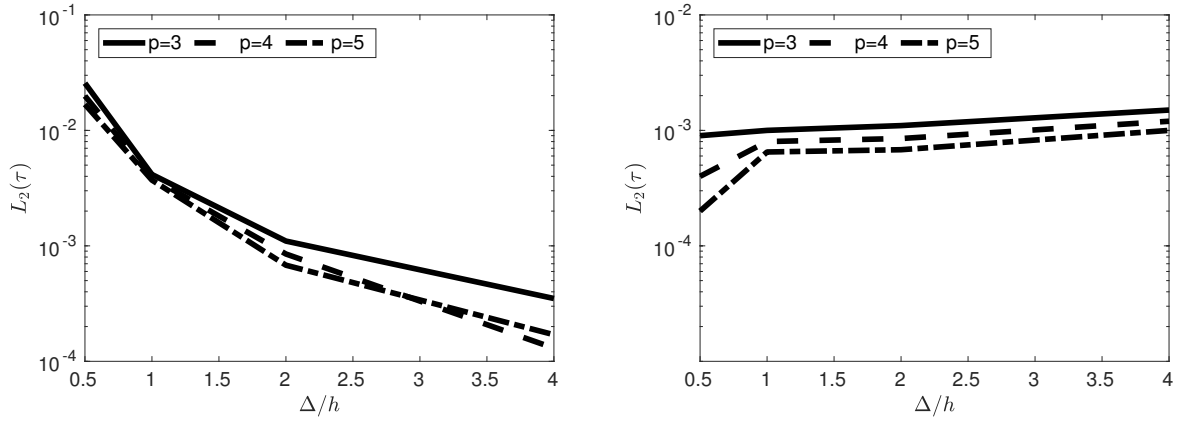

(a) (b)

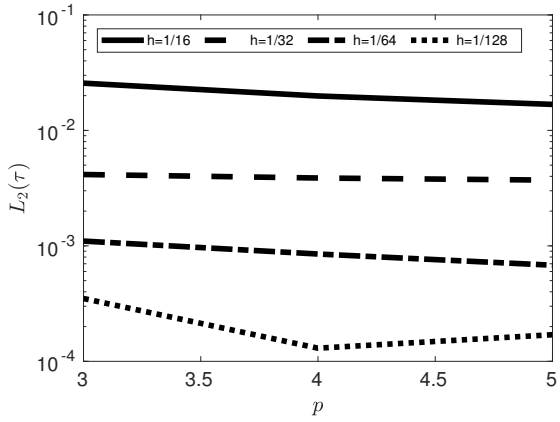

(c)

Figure 17: L_2 norm error analysis on SGS scalar variance. (a) fixed $\Delta = 1/32$, (b) fixed $h = 1/64$, (c) fixed $\Delta = 1/32$.

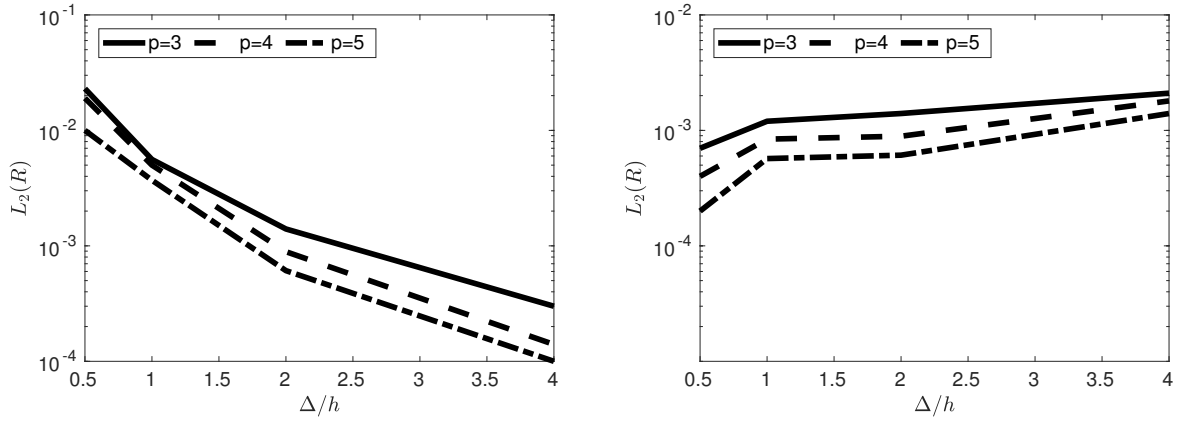

(a)

(b)

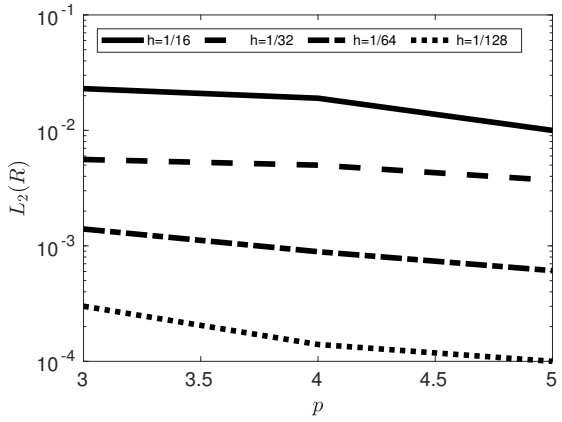

(c)

Figure 18: L_2 norm error analysis on resolved scalar variance. (a) fixed $\Delta = 1/32$, (b) fixed $h = 1/64$, (c) fixed $\Delta = 1/32$.

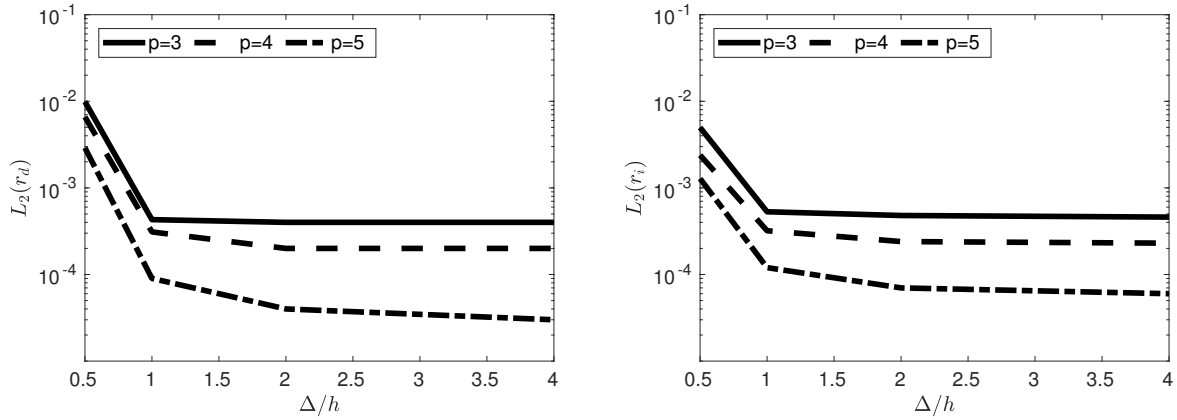

(a)

(b)

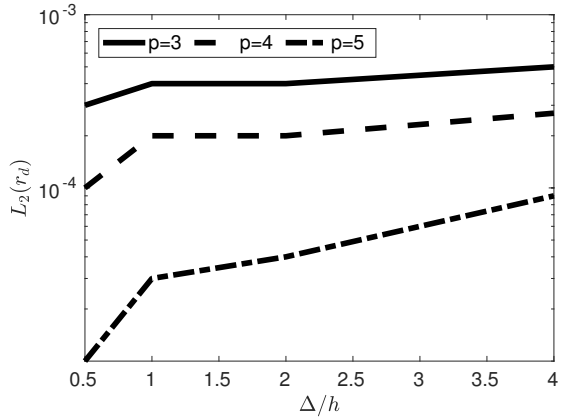

(c)

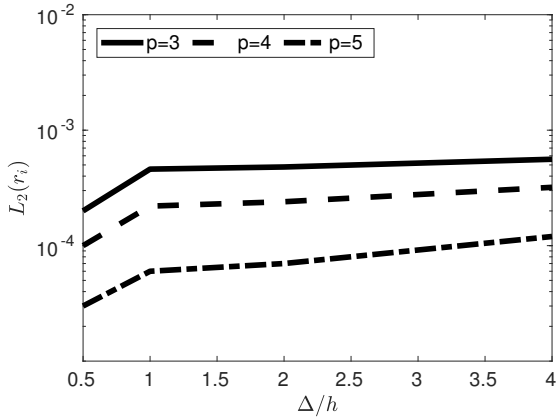

(d)

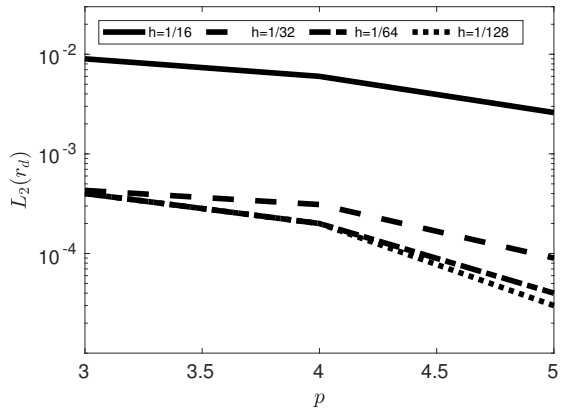

(e)

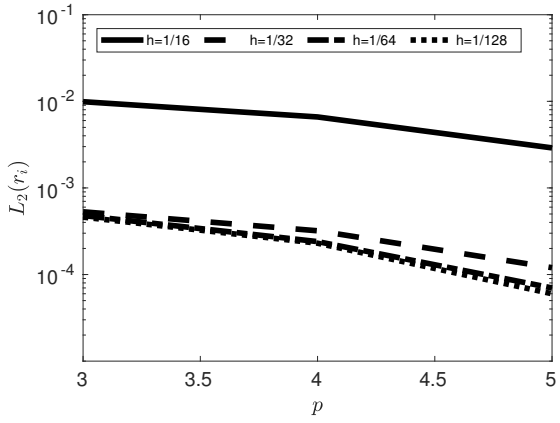

(f)

Figure 19: L_2 norm error analysis on total scalar variance. (a) direct method: fixed $\Delta = 1/32$, (b) indirect method: fixed $\Delta = 1/32$, (c) direct method: fixed $h = 1/64$, (d) indirect method: fixed $h = 1/64$, (e) direct method: fixed $\Delta = 1/32$, (f) indirect method: fixed $\Delta = 1/32$.

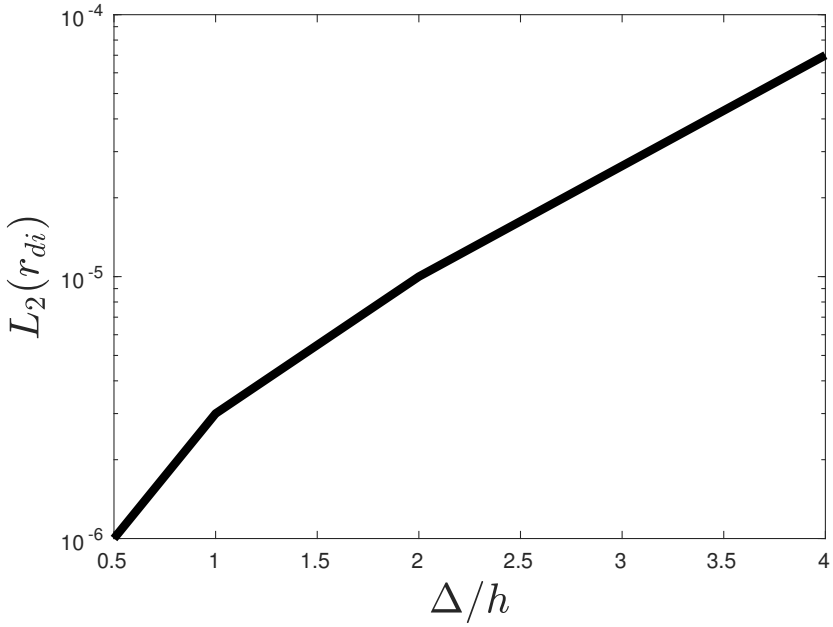

Figure 20: L_2 norm error of total scalar from DNS.

for the resolved variances. As expected of a successful LES, a more significant portion of the energy is resolved for a more accurate solution. In all of the cases, the total energy remains the same (Fig. 19) and for all p values, the LES predictions are in close agreements with the both filtered and unfiltered DNS data. This is very encouraging as it indicates that regardless of the portion of energy captured by the resolved field, the total energy is predicted well and there is no contamination of the total field due to SGS modeling.

Overall, for different values of Δ/h, LES results are in good agreement with DNS data, confirming that the resolution of $h = 1/64$ is sufficient. It also validates that the SGS model employed is capable of capturing the physics of the flow reasonably accurate. For SGS variance, resolved and total scalar, the LES results merges to the DNS results as the size of Δ decreases. Recall the model of SGS viscosity, the filter size Δ acts similar to the Smagorinsky constant. Adjusting the filter size is essentially modifying the SGS model.

The effect of the filter size on the total scalar variance is shown in Fig. 20. It is shown that for smaller Δ/h values, the assumption of generic filter is satisfied. Figure 21 indicates

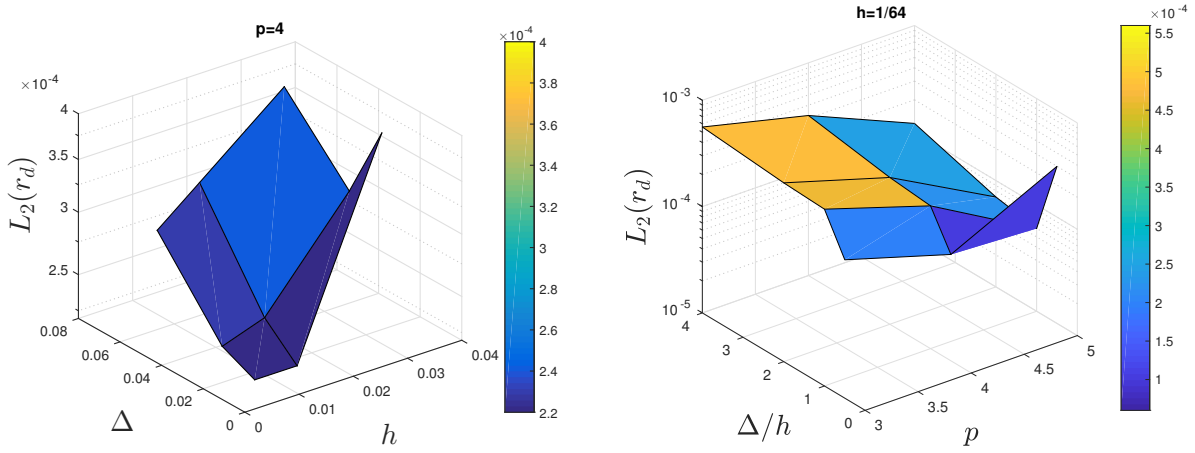

(a) (b)

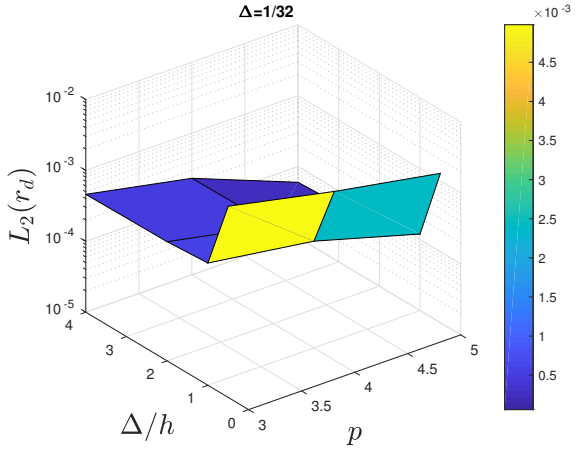

(c)

Figure 21: L_2 norm error of the total scalar variance from direct method: (a) fixed $p = 4$, (b) fixed $h = 1/64$, (c) fixed $\Delta = 1/32$.

a significant error reduction as p increases. However, decreasing the h from 1/64 to 1/128 does not portray any significant effects (Fig. 21(a)). At this point, it is important to indicate that the computational requirements become more significant with h-refinement. Reducing the grid size by a factor of 2 requires 2^4 more computational times. The increase of p from 3 to 4 and 5 increases the computational time by $\sim$5 and $\sim$8 times, respectively.

4.0 CONCLUDING REMARKS

A systematic study is conducted of the resolution requirements for large eddy simulation of turbulent flow, via the discontinuous Galerkin (DG) method. The subgrid scale model in LES is constructed based on the filtered density function. The resolution study is focused on the effects of element size (h), spectral polynomial approximation (p) and the LES filter width (Δ). The simulations indicate: (1) For fixed values of h and p, as Δ decreases, the LES predictions converge to DNS results. (2) For a fixed Δ, LES results converge to a grid-independent solution as h decreases or p increases. (3) For all values of Δ/h, DNS and LES results are in good agreements in predicting the magnitude of the total energy. (4) As the size of Δ decreases, the resolved and total energy values in LES converge to those from DNS. (5) For a fixed filter width, $p-$ refinement is shown to be more effective compared to $h-$ refinement as the order of accuracy converges exponentially for the former and computation cost are higher for the latter.

In general, $p-$ refinement gives a better convergence rate and requires relatively less computational times compared to $h-$ refinement. Therefore, we suggest that to improve the LES results, the best practice is to make the refinement via p, while keeping $\Delta \approx h$.

4.1 FUTURE WORK

We have achieved the basic guideline of choosing the important parameters in DG-LES, based on simulations of two-dimensional and three-dimensional mixing layers, with uniform mesh. For future work, we have the following suggestions:

1. Since the filter width plays a central role in the modeling of the unresolved stresses, it will be useful if different SGS models are tested.
2. Since the relationship between h and Δ is very important in simulations with non-uniform meshes, it is important to consider more complex geometries.
3. To develop a more physically consistent model, it is of interest to study the adaptive LES proposed by Pope [32], in which a measure of turbulence resolution (*e.g.* the percentage of unresolved energy or dissipation) is the only specified quantity, and the grid and filter width are adapted to achieve this.
4. The current work is limited to Newtonian fluids. It will be useful to also investigate turbulent flows of non-Newtonian fluids.

APPENDIX A

DG FORMULATION

The governing equations (Navier-Stokes equations) of compressible fluids are the conservation of mass, momentum, and energy, given as:

$$\frac{\partial U_k}{\partial t} + \frac{\partial F_{ki}}{\partial x_i} = 0, \tag{A.1}$$

where U is the solution vector, and F represents the flux, defined as:

$$U = \begin{Bmatrix} \rho \\ \rho u \\ \rho v \\ \rho w \\ \rho E \end{Bmatrix}, \quad F = \begin{Bmatrix} \rho u & \rho v & \rho w \\ \rho u^2 + P - \tau_{11} & \rho uv - \tau_{12} & \rho uw - \tau_{13} \\ \rho uv - \tau_{21} & \rho v^2 + P - \tau_{22} & \rho vw - \tau_{23} \\ \rho uw - \tau_{31} & \rho vw - \tau_{32} & \rho w^2 + P - \tau_{33} \\ \rho uH - \tau_{1j}u_j + q_1 & \rho vH - \tau_{2j}u_j + q_2 & \rho wH - \tau_{3j} + q_3 \end{Bmatrix}, \tag{A.2}$$

where ρ is the density, u, v, w are the velocity components in each spatial coordinate direction, P is the pressure, E is total internal energy, $H = E + P/\rho$ is the total enthalpy, τ is the viscous stress tensor, and q is the heat flux. The viscosity is a function of the temperature given by the Sutherland's formula. These equations are closed using the ideal gas equation of state:

$$\rho E = \frac{P}{\gamma - 1} + \frac{1}{2}\rho\left(u^2 + v^2 + w^2\right), \tag{A.3}$$

where $\gamma = 1.4$ is the ratio of specific heats. Einstein notation is used in all of the following where the subscripts of i and j respresent spatial dimensions from 1 to 3. The index k varies over the number of variables.

To derive the weak form, Eq. (A.1) is first multiplied by a test function ϕ and integrated over the domain Ω to give:

$$\int_{\Omega} \phi_m \left(\frac{\partial U_k}{\partial t} + \frac{\partial F_{ki}}{\partial x_i} \right) \, \mathrm{d}\Omega = 0. \tag{A.4}$$

Integrate it by parts and the residual R_{nm} is defined as:

$$R_{km} = \int_{\Omega} \left(\phi_m \frac{\partial U_k}{\partial t} - \frac{\partial \phi_m}{\partial x_i} F_{ki} \right) \, \mathrm{d}\Omega + \int_{\Gamma} F_{ki} n_i \, \mathrm{d}\Gamma = 0, \tag{A.5}$$

where ϕ are the basis functions and the solution is approximated using $U_k = \phi_m a_{km}$. The index m runs over the number of basis functions. The advective fluxes are calculated using a Riemann solver. The implemented Riemann solvers include: Lax-Friedrichs [64], Roe [65], and artificially upstream flux vector splitting scheme (AUFS) [66]. The diffusive fluxes are handled using a symmetric interior penalty (SIP) method [67, 68].

To solve the non-linear set of equations, a damped Newton's method is used:

$$\mathbf{J}^k \Delta a^k = \left[\frac{\mathbf{M}}{\Delta t} + \left(\frac{\partial R}{\partial a} \right)^k \right] \Delta a^k = -R^k, \tag{A.6}$$

where k is the non-linear iteration, $\mathbf{J}$ is the Jacobian matrix, $\mathbf{M}$ is a mass matrix and Δt is an element-wise time step which is used to dampen the solution of the linear update problem. The mass matrix $\mathbf{M}$ only appears on the block diagonals due to the discontinuous basis. A local time step Δt is set on every element using

$$\Delta t = \frac{CFL}{h^{-1}(\sqrt{u^2 + v^2 + w^2} + c)}, \tag{A.7}$$

where h is a mesh size and c is the speed of sound. The CFL number is not based on an explicit stabilit limit, but rather is used to control the convergence characteristic of the implicit scheme. Newton's method creates a linear system that must be solved to get the update to the coefficients a_{ns} by:

$$a^{k+1} = a^k + \Delta a^k. \tag{A.8}$$

To solve the linear system in Eq. (A.6), a flexible-GMRES [69] (fGMRES) method is used. To further improve convergence of fGMRES, a preconditioner P can be applied to the system of equations, which in this work takes the form:

$$\mathbf{A}\mathbf{P}^{-1}\mathbf{z} = \mathbf{b}, \mathbf{z} = \mathbf{P}\mathbf{x}. \tag{A.9}$$

Preconditioners that have been implemented include Jacobi relaxation, Gauss-Seidel relaxation, line implicit Jacobi, and ILU(0).

APPENDIX B

ERROR ESTIMATE STUDY OF DG

The two-dimensional Ringleb flow is considered as a test case to provide an error estimation of the DG implementation. Ringleb is a two-dimensional exact solution to the Euler equations. This exact solution is suitable for testing the order of accuracy of the solver. The L_2 error norm is used:

$$L_2 = \frac{\left[\Sigma_{i=1}^{n_{cell}} \int_\Omega (u - u_e)^2 \ \mathrm{d}\Omega\right]^{1/2}}{\Sigma_{i=1}^{n_{cell}} V_i},$$

where V is the volume of each cell, u is from the DG solver and u_e the exact solution.

Simulations are conducted with four different mesh sizes h, consisting of 5, 10, 20 and 40 elements in both flow directions. The simulated results are compared with the exact solution. The L_2 norm of the error for the four sets of grids and polynomial degrees ranging from $p = 0$ to $p = 3$ is presented in Fig. 22. It is shown that the error decreases as predicted in a rate proportional to h^{p+1} or better. This is a demonstration that the DG solver maintains the correct order of accuracy.

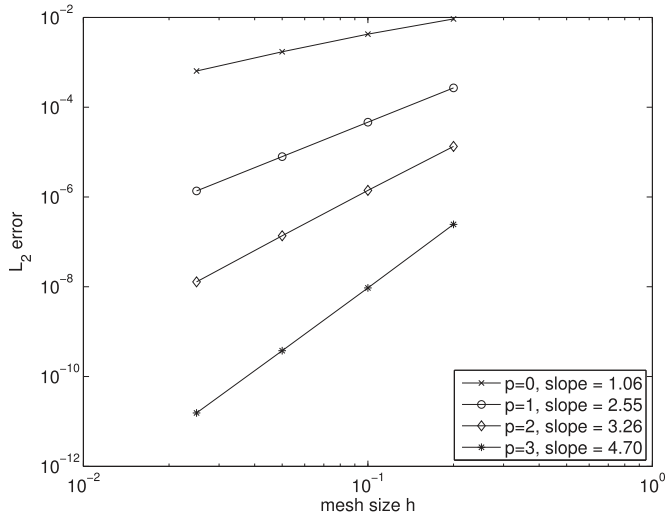

Figure 22: L_2 norm errors of DG for different mesh size h.

BIBLIOGRAPHY

[1] McMurthy, P. A., Menon, S., and Kerstein, A. R., A Linear Eddy Sub-grid Model for Turbulent Reacting Flows: Application to Hydrogen-AIR Combustion, *Proc. Combust. Inst.*, **24**(1):271 – 278 (1992).

[2] Menon, S., McMurtry, P. A., and Kerstein, A. K., *Large Eddy Simulation of Complex Engineering and Geophysical Flows*, Chapter A Linear Eddy Sugbrid Model of Turbulent Combustion, pp. 287–314, Cambridge University Press, Cambridge, UK, 1993.

[3] Gao, F. and O'Brien, E. E., A Large-eddy Simulation Scheme for Turbulent Reacting Flows, *Phys. Fluids A*, **5**(6):1282–1284 (1993).

[4] Madnia, C. K. and Givi, P., *Large Eddy Simulation of Complex Engineering and Geophysical Flows*, Chapter Direct Numerical Simulation and Large Eddy Simulation of Reacting Homogeneous Turbulence, pp. 315–346, Cambridge University Press, Cambridge, UK, 1993.

[5] Cook, A. W. and Riley, J. J., A Subgrid Model for Equilibrium Chemistry in Turbulent Flows, *Phys. Fluids*, **6**(8):2868–2870 (1994).

[6] Jaberi, F. A. and James, S., A Dynamic Similarity Model for Large Eddy Simulation of Turbulent Combustion, *Phys. Fluids*, **10**(7):1775–1777 (1998).

[7] Pope, S. B., Small Scales, Many Species and the Manifold Challenges of Turbulent Combustion, *Proc. Combust. Inst.*, **34**(1):1–31 (2013).

[8] Foster, J. W. and Miller, R. S., Survey of Turbulent Combustion Models for Large-eddy Simulations of Propulsive Flowfields, in *53rd AIAA Aerospace Sciences Meeting*, Kissimmee, FL, 2015, AIAA 2015-1379.

[9] Rogallo, R. S. and Moin, P., Numerical Simulation of Turbulent Flows, *Annu. Rev. Fluid Mech.*, **16**:99–137 (1984).

[10] Givi, P., Filtered Density Function for Subgrid Scale Modeling of Turbulent Combustion, *AIAA J.*, **44**(1):16–23 (2006).

[11] Moin, P. and Jimenez, J., Large Eddy Simulation of Complex Flows, in *24th AIAA Fluid Dynamics Conference*, Orlando, FL, 1993, AIAA 93-3099.

[12] Smagorinsky, J., General Circulation Experiments with the Primitive Equations. I. The Basic Experiment, *Mon. Weather Rev.*, **91**(3):99–164 (1963).

[13] Bardina, J., Ferziger, J. H., and Reynolds, W. C., Improved Turbulence Models Based on Large Eddy Simulation of Homogeneous, Incompressible Turbulent Flows, Technical report, Stanford University, 1983, Thermosciences Division TF-19.

[14] Liu, S., Meneveau, C., and Katz, J., On the Properties of Similarity Subgrid-Scale Models as Deduced from Measurements in a Turbulent Jet, *J. Fluid Mech.*, **275**:83–119 (1994).

[15] Clark, R. A., Ferziger, J. H., and Reynolds, W. C., Evaluation of Subgrid-scale Models Using an Accurately Simulated Turbulent Flow, *J. Fluid Mech.*, **91**(1):1–16 (1979).

[16] Germano, M., Turbulence: the Filtering Approach, *J. Fluid Mech.*, **238**:325–336 (1992).

[17] Zang, Y., Street, R. L., and Koseff, J. R., A Dynamic Mixed Subgrid-scale Model and Its Application to Turbulent Recirculating Flows, *Phys. Fluids A*, **5**(12):3186–3196 (1993).

[18] Vreman, B., Geurts, B., and Kuerten, H., On the Formulation of the Dynamic Mixed Subgrid-scale Model, *Phys. Fluids*, **6**(12):4057–4059 (1994).

[19] Vreman, B., Geurts, B., and Kuerten, H., Large-eddy Simulation of the Temporal Mixing Layer Using the Clark Model, *Theor Comp. Fluid Dyn.*, **8**(4):309–324 (1996).

[20] Vreman, B., Geurts, B., and Kuerten, H., Large-Eddy Simulation of the Turbulent Mixing Layer, *J. Fluid Mech.*, **339**:357–390 (1997).

[21] Kuo, K. K. and Acharya, R., *Fundamentals of Turbulent and Multiphase Combustion*, John Wiley and Sons Inc., Hoboken, NJ, 2012.

[22] Poinsot, T. and Veynante, D., *Theoretical and Numerical Combustion*, R.T. Edwards, Inc., Philadelphia, PA, second edition, 2005.

[23] Janicka, J. and Sadiki, A., Large Eddy Simulation of Turbulent Combustion Systems, *Proc. Combust. Inst.*, **30**(1):537–547 (2005).

[24] Pope, S. B., *Turbulent Flows*, Cambridge University Press, Cambridge, U.K., 2000.

[25] Bilger, R. W., Future Progress in Turbulent Combustion Research, *Prog. Energ. Combust.*, **26**(4–6):367–380 (2000).

[26] Peters, N., *Turbulent Combustion*, Cambridge University Press, Cambridge, UK, 2000.

[27] Givi, P., Model-free Simulations of Turbulent Reactive Flows, *Prog. Energy Combust. Sci.*, **15**(1):1–107 (1989).

[28] Pope, S. B., Computations of Turbulent Combustion: Progress and Challenges, *Proc. Combust. Inst.*, **23**(1):591–612 (1990).

[29] Nik, M. B., VS-FMDF and EPVS-FMDF for Large Eddy Simulation of Turbulent Flows, Ph.D. Thesis, Department of Mechanical Engineering and Materials Science, University of Pittsburgh, Pittsburgh, PA, 2012.

[30] Nouri, A. G., Nik, M. B., Givi, P., Livescu, D., and Pope, S. B., Self-contained Filtered Density Function, *Phys. Rev. Fluids*, **2**(9):094603 (2017).

[31] Drummond, J. P., Methods for Prediction of High-Speed Reacting Flows in Aerospace Propulsion, *AIAA J.*, **52**(3):465–485 (2014).

[32] Pope, S. B., Ten Questions Concerning the Large-eddy Simulation of Turbulent Flows, *New J. Phys.*, **6**:35–35 (2004).

[33] Vreman, B., Geurts, B., and Kuerten, H., Comparison of Numerical Schemes in Large-eddy Simulation of the Temporal Mixing Layer, *Int. J. Numer. Methods Fluids*, **22**(4):297–311 (1996).

[34] Meyers, J., Geurts, B. J., and Baelmans, M., Database Analysis of Errors in Large-eddy Simulation, *Phys. Fluids*, **15**(9):2740–2755 (2003).

[35] Ghosal, S., An Analysis of Numerical Errors in Large-Eddy Simulations of Turbulence, *J. Comput. Phys.*, **125**(1):187 – 206 (1996).

[36] Chow, F. K. and Moin, P., A Further Study of Numerical Errors in Large-eddy Simulations, *J. Comput. Phys.*, **184**(2):366 – 380 (2003).

[37] Geurts, B. J. and Fröhlich, J., *Modern Simulation Strategies for Turbulent Flow*, Chapter Numerical Effects Contaminating LES: A Mixed Story, pp. 309–327, R.T. Edwards, Inc., Ann Arbor, MI, 2001.

[38] Geurts, B. J. and Fröhlich, J., A Framework for Predicting Accuracy Limitations in Large-eddy Simulation, *Phys. Fluids*, **14**(6):L41–L44 (2002).

[39] Sammak, S., Brazell, M. J., Givi, P., and Mavriplis, D. J., A Hybrid DG-Monte Carlo FDF Simulator, *Comput. Fluids*, **140**:158–166 (2016).

[40] Sammak, S., Brazell, M. J., Mavriplis, D. J., and Givi, P., Discontinuous Galerkin-Monte Carlo Solver for Large Eddy Simulation of Compressible Turbulent Flows, in *AIAA Aerospace Sciences Meeting*, Grapevine, TX, 2017, AIAA, AIAA 2017-0982.

[41] Brazell, M. and Mavriplis, D. J., 3D Mixed Element Discontinuous Galerkin with Shock Capturing, in *21st AIAA CFD Conference*, San Diego, CA, 2013, AIAA, AIAA 2013-2855.

[42] Wang, L. and Mavriplis, D. J., Adjoint Based h-p Adaptive Discontinuous Galerkin Methods for Aerospace Applications, in *AIAA Aerospace Sciences Meeting*, Orlando, FL, 2009, AIAA, AIAA-2009-0952.

[43] Piomelli, U., Large-eddy Simulation: Achievements and Challenges, *Prog. Aerosp. Sci.*, **35**(4):335–362 (1999).

[44] Grinstein, F. F., Margolin, L. G., and Rider, W. J., *Implicit Large Eddy Simulation: Computing Turbulent Fluid Dynamics*, Cambridge University Press, New York, NY, 2007.

[45] Sagaut, P., *Large Eddy Simulation for Incompressible Flows: An Introduction*, Springer, Berlin, Heidelberg, 2006.

[46] Smagorinsky, J., General Circulation Experiments with the Primitive Equations. I. The Basic Experiment, *Mon. Weather Rev.*, **91**(3):99–164 (1963).

[47] Ghosal, S. and Moin, P., The Basic Equations for the Large Eddy Simulation of Turbulent Flows in Complex Geometry, *J. Comput. Phys.*, **118**(1):24–37 (1995).

[48] O'Brien, E. E., The Probability Density Function (PDF) Approach to Reacting Turbulent Flows, in Libby, P. and Williams, F., editors, *Turbulent Reacting Flows*, *Topics in Applied Physics*, Vol. 44, Chapter 5, pp. 185–218, Springer, Berlin, Heidelberg, 1980.

[49] Pope, S. B., PDF Methods for Turbulent Reactive Flows, *Prog. Energ. Combust.*, **11**(2):119–192 (1985).

[50] Vreman, B., Geurts, B., and Kuerten, H., Realizability Conditions for the Turbulent Stress Tensor in Large-eddy Simulation, *J. Fluid Mech.*, **278**:351–362 (1994).

[51] Colucci, P. J., Jaberi, F. A., Givi, P., and Pope, S. B., Filtered Density Function for Large Eddy Simulation of Turbulent Reacting Flows, *Phys. Fluids*, **10**(2):499–515 (1998).

[52] Jaberi, F. A., Colucci, P. J., James, S., Givi, P., and Pope, S. B., Filtered Mass Density Function for Large-Eddy Simulation of Turbulent Reacting Flows, *J. Fluid Mech.*, **401**:85–121 (1999).

[53] Gikhman, I. I. and Skorokhod, A. V., *Stochastic Differential Equations*, Springer-Verlag, New York, NY, 1972.

[54] Risken, H., *The Fokker-Planck Equation, Methods of Solution and Applications*, Springer-Verlag, New York, NY, 1989.

[55] Brazell, M., Sitaraman, J., and Mavriplis, D. J., An Overset Mesh Approach for 3D Mixed Element High Order Discretizations, in *53rd AIAA Aerospace Sciences Meeting*, Kissimmee, FL, 2015, AIAA, AIAA 2015-1739.

[56] Comte, P., Lesieur, M., and Lamballais, E., Large-and Small-scale Stirring of Vorticity and a Passive Scalar in a 3-D Temporal Mixing Layer, *Phys. Fluids A*, **4**(12):2761–2778 (1992).

[57] Rogers, M. M. and Moser, R. D., Direct Simulation of a Self-similar Turbulent Mixing Layer, *Phys. Fluids*, **6**(2):903–923 (1994).

[58] Luo, K. H. and Sandham, N. D., On the Formation of Small Scales in a Compressible Mixing Layer, in *Direct and Large-Eddy Simulation I*, pp. 335–346, Dordrecht, Netherlands, 1994, Springer.

[59] Vreman, A. W., Sandham, N. D., and Luo, K. H., Compressible Mixing Layer Growth Rate and Turbulence Characteristics, *J. Fluid Mech.*, **320**:235–258 (1996).

[60] Jameson, A., Schmidt, W., and Turkel, E., Numerical Solution of the Euler Equations by Finite Volume Methods Using Runge Kutta Time Stepping Schemes, in *14th AIAA Fluid and Plasma Dynamics Conference*, Palo Alto, CA, 1981, AIAA, AIAA 1981-1259.

[61] Vreman, B., Geurts, B., and Kuerten, H., Realizability Conditions for the Turbulent Stress Tensor in Large-Eddy Simulation, *J. Fluid Mech.*, **278**:351–362 (1994).

[62] Sheikhi, M. R. H., Givi, P., and Pope, S. B., Velocity-Scalar Filtered Mass Density Function for Large Eddy Simulation of Turbulent Reacting Flows, *Phys. Fluids*, **19**(9):095106 (2007).

[63] Sammak, S., Brazell, M. J., Givi, P., and Mavriplis, D. J., A Hybrid DG-Monte Carlo FDF Simulator, *Comput. Fluids*, **140**(13):158–166 (2016).

[64] Lax, P. D., Weak Solutions of Nonlinear Hyperbolic Equations and Their Numerical Computation, *Comm. Pure Appl. Math.*, **7**(1):159–193 (1954).

[65] Roe, P. L., Approximate Riemann Solvers, Parameter Vectors and Difference Dchemes, *J. Comput. Phys.*, **43**(2):357–372 (1981).

[66] Sun, M. and Takayama, K., An Artificially Upstream Flux Vector Splitting Scheme for the Euler Equations, *J. Comput. Phys.*, **189**(1):305–329 (2003).

[67] Shahbazi, K., Mavriplis, D. J., and Burgess, N. K., Multigrid Algorithms for High-order Discontinuous Galerkin Discretizations of the Compressible Navier-Stokes Equations, *J. Comput. Phys.*, **228**(21):7917–7940 (2009).

[68] Hartmann, R. and Houston, P., An Optimal Order Interior Penalty Discontinuous Galerkin Discretization of the Compressible Navier-Stokes Equations, *J. Comput. Phys.*, **227**(22):9670–9685 (2008).

[69] Saad, Y., A Flexible Inner-Outer Ppreconditioned GMRES Algorithm, *SIAM J. Sci. Comput.*, **14**(2):461–469 (1993).